The Role of the Interfaces in Perovskite Solar Cells

Shao, Shuyan; Loi, Maria Antonietta

Published in:
Advanced Materials Interfaces

DOI:
10.1002/admi.201901469

Publication date:
2020

ADVANCED MATERIALS INTERFACES
www.advmatinterfaces.de

The Role of the Interfaces in Perovskite Solar Cells

*Shuyan Shao and Maria Antonietta Loi**

Organic–inorganic hybrid perovskite solar cells (HPSCs) have achieved an impressive power conversion efficiency (PCE) of 25.2% in 2019. At this stage, it is of paramount importance to understand in detail the working mechanism of these devices and which physical and chemical processes govern not only their power conversion efficiency but also their long-term stability. The interfaces between the perovskite film and the charge transport layers are among the most important factors in determining both the PCE and stability of HPSCs. Herein, an overview is provided on the recent advances in the fundamental understanding of how these interfaces influence the performance of HPSCs. Firstly, it is discussed how the surface energy of the charge transport layer, the energy level alignment at the interfaces, the charge transport in interfacial layers, defects and mobile ions in the perovskite film, and interfacial layers or at the interfaces affect the charge recombination as well as hysteresis and light soaking phenomenon. Then it is discussed how the interfaces and interfacial materials influence the stability of HPSCs. At the same time, an overview is also provided on the various design strategies for the interfaces and the interfacial materials. At the end, the outlook for the development of highly efficient and stable HPSCs is provided.

1. Introduction

The frequent energy crisis and the climate change caused by the massive consumption of fossil fuels are challenging the future of the development of human civilization. The development of alternative clean and renewable energy sources to help reducing CO_2 emission has become a common global goal. Several alternative energy sources such as wind, water, solar and nuclear energy have been proposed to generate electricity as alternatives to fossil fuels. Among these energy sources, solar energy is an ideal candidate due to its environmental friendliness and abundance. Photovoltaic (PV) technology, which directly converts the solar energy into electrical energy, is one of the several technologies allowing exploiting solar energy. How to improve the efficiency of the solar energy harvesting at low cost is nowadays an important research subject both for academia and industry. However, at the moment, the energy produced by solar cells is less than 1% of the global demand. One of the main reasons is the high investment needed for KW h^{-1}, which is mostly due to the complex production process and high material consumption and the relatively low efficiency for the state-of-art crystalline silicon-based solar cells, which claims 90% of the global market share. While the second generation of thin film PVs accounts roughly for 9% of the market share and is mostly limited by the high cost due to the use of rare and toxic elements.

The third-generation thin film solar cell technologies fabricated through solution-processable techniques, such as organic photovoltaics (OPVs), dye-sensitized solar cells (DSSCs), quantum-dot solar cells (QDSCs) have the advantages of the potential low cost, and light weight. However, these solar cells are still struggling with the low power conversion efficiency (PCE < 20%) over more than one decade development, which is most probably due to the compromise between the light absorption and the charge collection.[1]

Metal halide perovskites have a ABX_3 crystal structure as shown in **Figure 1**, where the cavity (A cite) is occupied by an monovalent organic or cation (Cs^+, $CH_3NH_3^+$, or $CH(NH_2)^+$); the body center (B site) of the octahedra is occupied by a divalent metal cation (Pb^{2+}, Sn^{2+}); and the corner (X site) of the octahedra is occupied by halide anions (Cl^-, Br^-, I^-).[2,3] This material family has excellent photophysical and electrical properties, such as the high absorption coefficient, very small exciton binding energy, the long charge carrier diffusion length, and the balanced charge carrier transport.[4–12] Furthermore, these materials have very good solution processability, compatible with the low cost fabrication techniques, such as roll-to-roll printing.[12–16] These characteristics make metal halide perovskites ideal candidates as light absorbing layers for high efficiency and low-cost PV technology.

In 2009, Miyasaka and co-workers pioneered in using the $CH_3NH_3PbI_3$ ($MAPbI_3$) and $MAPbBr_3$ as sensitizer in liquid electrolyte based DSSCs, showing PCEs of 3.8%, and 3.1%, respectively.[17] In 2011, Park and co-workers further improved

Dr. S. Shao, Prof. M. A. Loi
Photophysics and OptoElectronics
Zernike Institute for Advanced Materials
University of Groningen
Nijenborgh 4, 9747 AG Groningen, The Netherlands
E-mail: m.a.loi@rug.nl

The ORCID identification number(s) for the author(s) of this article can be found under https://doi.org/10.1002/admi.201901469.

DOI: 10.1002/admi.201901469

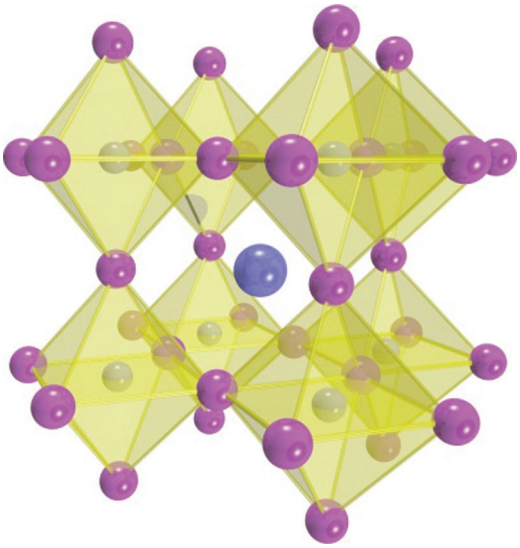

Figure 1. Cubic perovskite crystal structure.

the PCE of the liquid-based $MAPbI_3$ solar cell to 6.5% by modifying the surface of TiO_2 and the deposition method for perovskite.[17] However, this approach had an evident drawback due to the dissolution of perovskite compounds in liquid electrolytes. To overcome these draw backs, the research shifted to solid state DSSCs, in which a solid hole conduction material was used to replace the liquid electrolyte. In 2012, Park et al. reported the first solid-state mesoscopic heterojunction perovskite solar cells (HPSCs) using sub-micrometer thick mesoporous TiO_2 film (0.6–1 µm) as electron transport layer (ETL), $MAPbI_3$ as light absorbers, and 2,2′,7,7′-tetrakis(N,N-di-p-methoxyphenylamine)-9,9′-spirobifluorene(spiro-OMeTAD) as hole transport layer (HTL) as shown in **Figure 2**a, a PCE of 9.7% with remarkably improved stability up to 500 h in air were recorded.[18] In the same year, Snaith and co-workers reported similar solid-state HPSCs structure using mesoporous TiO_2 as electron transport material, spiro-OMeTAD as HTL and mixed halide perovskite ($CH_3NH_3PbI_2Cl$) as a light absorbing layer. A PCE of 10.8% was achieved by replacing the mesoporous TiO_2 structure with the insulating Al_2O_3 (Figure 2b), which functions as scaffold and helps to reduce the chemical capacitance in the device.[19] This indicates that the perovskite layer itself is good electron transport material, but the first trials of planar device structures (Figure 2d) displayed a very low PCE of 1.8%. Almost in the same period, Grätzel and co-workers reported a PCE of 5.5% for a hole-conductor free mesoporous HPSC using a TiO_2 sheet as electron transport layer, $CH_3NH_3PbI_3$ as light absorber layer, and Au as anode (Figure 2c).[20] This confirmed that the perovskite active layer could also transport holes. Kelly and co-workers demonstrated an ETL free HPSC with a planar heterojunction with an efficiency of 13.5% (Figure 2e).[21] However, the absence of the ETL or HTL in the cell determines stability issues or large hysteresis due to the poor charge extraction, which highlights the importance of the hole or electron selective layers on the performance of the HPSCs. In 2013, Snaith and co-workers further improved the PCE to 12.3% by reducing the Al_2O_3 layer thickness and the processing temperature.[22]

Shuyan Shao received her BS degree in Polymer Materials and Engineering in 2006 from Hebei University in China. In 2011, she received her PhD degree at Changchun Institute of Applied Chemistry, Chinese Academy of Science, China. In July of the same year, she joined Linköping University as a postdoctoral researcher. Since 2014, she has been a Marie Curie Research Fellow and postdoctoral research fellow in University of Groningen. Her current research topics include perovskite solar cells, field effect transistors and memristors.

Maria Antonietta Loi studied physics at the University of Cagliari in Italy where she received the PhD in 2001. In the same year, she joined as a postdoctoral fellow the Linz Institute for Organic Solar cells, of the University of Linz, Austria. Later she worked as a researcher at the Institute for Nanostructured Materials of the Italian National Research Council in Bologna, Italy. In 2006, she became an assistant professor and Rosalind Franklin Fellow at the Zernike Institute for Advanced Materials of the University of Groningen, The Netherlands. Since 2014, she is a full professor and chair of Photophysics and OptoElectronics in the same institution.

In parallel to the mesoscopic structure, they also improved the PCE of the planar n–i–p device structure to 5%. In 2013, Wen and co-workers reported the first p–i–n planar device structure (Figure 2f) and got a PCE of 3.8%.[23] Later in the same year, Snaith and co-workers successfully improved the PCE of an n–i–p planar HPSC to 15.4%, in this device the perovskite film was formed by vapor deposition.[24] With the same device structure, by using a solution processed perovskite film the efficiency was down to 8%. The discrepancy in the performance of these devices was attributed to the difference in the morphology, where vapor deposition gives extremely uniform and compact perovskite films, while solution processing produces noncompact films. This remarkable device performance further demonstrated that the mesoscopic structure is not necessary for high efficiency HPSCs. This is because the charge carriers can reach the respective anode/cathode within their lifetime as evidenced by studies on the charge carrier recombination dynamics. Optical spectroscopy studies indicated that holes and electrons have long

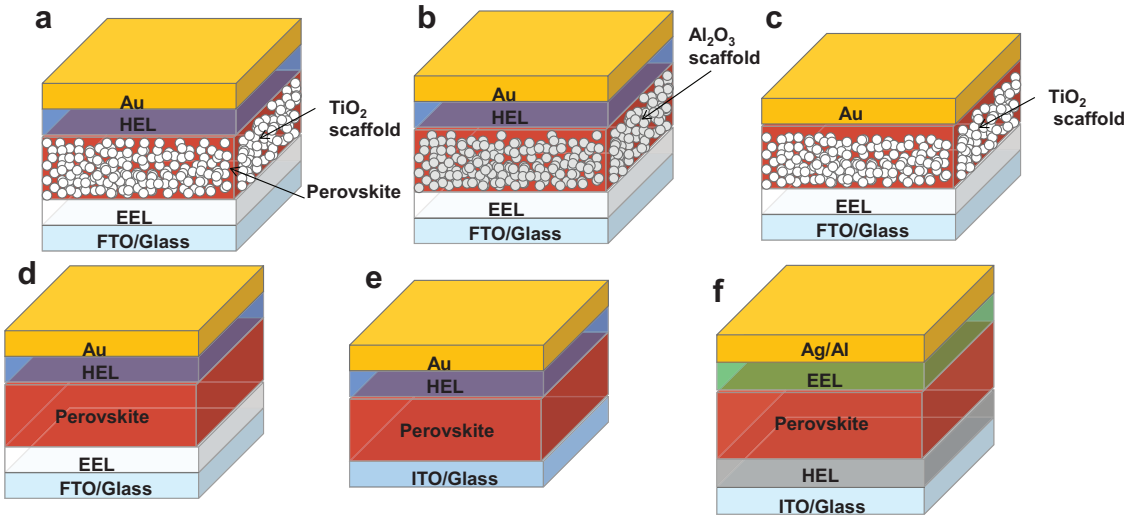

Figure 2. Device structures of HPSCs. a) mesoporous structure with TiO_2 as scaffold, b) mesoporous device structure with Al_2O_3 as scaffold, c) mesoporous structure without HTL, d) planar n–i–p device structure, e) planar device structure without ETL, f) planar p–i–n device structure.

lifetime and diffuse for distances over 1 µm in the perovskite film.[5,25] Time-resolved microwave conductivity (TRMC) and terahertz photoconductivity measurements indicated high charge carrier mobility and balanced charge transport.[25,26] Moreover, because of the high absorption coefficient, almost full absorption of the incident light is obtained already for films with a thickness 500–600 nm.

The unique photophysical and electrical properties of perovskite stimulated extensive research efforts aimed at the developments of new device structures, improved deposition methods, new interfacial layers, tailored chemical composition, and interface engineering all aimed to improve device PCE and stability.[27–55] Thanks to the great efforts of the large community, lead- based HPSCs (single junction) have achieved a certified efficiency of 25.2% in 2019.[56]

From the brief history of HPSCs highlighted above, it is evident that the majority of the high efficiency devices have a sandwich structure, with four different interfaces, namely, the perovskite/ETL interface, perovskite/HTL interface, ETL/cathode interface, and HTL/anode interface. These interfaces together with the interfacial materials have a very important role in the operation of the HPSCs determining their electronic properties.[57–59] Herein, we provide an overview of the recent advances in the fundamental understanding of how these interfaces influence the performance of perovskite solar cells. More specifically, we discuss the effects of interface engineering on the perovskite film morphology, the energy level alignment at perovskite/HTL (ETL) and ETL/cathode interfaces, and the charge transport in HTL (ETL) materials, and how they synergetically determine charge transport and extraction processes and thus the ultimate performance of the solar cells. In addition, the effects of these interfaces on the hysteresis and light soaking effect are also reviewed. We further discuss how the interfaces and interfacial materials affect the stability of the HPSCs when they are exposed to moisture, oxygen/light, and to temperature stress. Last, we also provide the outlook and highlight the key challenges and future directions for designing interfaces toward highly efficient and stable PSCs.

2. The Role of the Interfaces

The charge generation, transport, collection, and recombination in HPSCs are depicted in **Figure 3**.[26,60,61] Upon absorption of light, free charge carriers with electrons in the conduction band (CB) and holes in the valence band (VB) are generated due to the very small effective exciton binding energy and the high permittivity of perovskites.[9,62] These photogenerated free holes/electrons drift to the perovskite/HTL or perovskite/ETL interfaces under built-in electric field. During the transport in the perovskite film, bulk recombination of the charge carrier occurs. A portion of the charge carriers can be trapped (k_T) by bulk traps and recombine with the opposite free charge carriers (first-order recombination, k_R, dominates especially at low charge carrier density). Part of the free electrons can also recombine with the free holes (the second-order recombination, k_2 dominates in the case of high charge carrier density). Here, we do not discuss Auger recombination (third-order recombination), which happens at much higher carrier density compared to the one sun condition. After crossing the active layer holes/electrons are transferred to HTL/ETL (k_h and k_e) across the

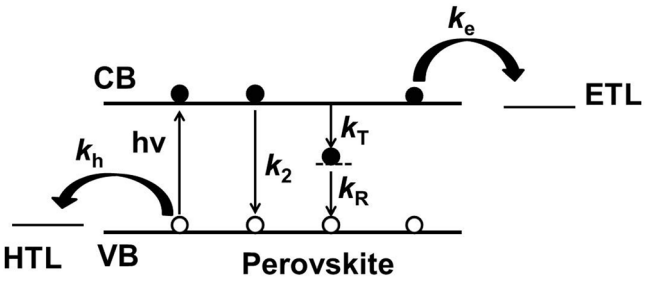

Figure 3. Schematic diagram of processes occurring in a sandwich structure of HTL/$MAPbI_3$/ETL. Electrons (black spheres) and holes (white spheres) are generated in the perovskite film upon absorption of light ($h\nu$). In the neat perovskite, electrons can recombine with holes via second-order band-to-band recombination (k_2), or get trapped (trap density N_T, trapping rate k_T) and recombine with holes via k_R. In the presence of an organic transport layer, electrons and holes can be injected via k_e and k_h, respectively.

perovskite/HTL and perovskite/ETL interfaces, where the interfacial recombination of the charge carriers takes place. The interfacial traps also cause first-order recombination,[50,51] while the charge accumulation at the interface due to the energy barrier or poor charge transport capability of the ETL or HTL causes second-order recombination.[30,63–65] Then the charge carriers are injected to the anode/cathode electrodes across the HTL/anode and ETL/cathode interfaces.

The energy barrier, the defects or charge/ion accumulation at perovskite/transport materials interfaces, ions in perovskite or charge transport layers, and charge mobility in charge transport layers not only determine the charge collection efficiency, but also have great impact on the hysteresis and light soaking effect in the HPSCs,[49,66] because they could enhance or screen the built in potential (depending on the type of species), enhancing or reducing the open-circuit voltage (V_{OC}) of the device.[49,52,67,68] Therefore, the interfaces and the interfacial materials need to be carefully engineered to avoid all the aforementioned problematic aspects.

In the following subsections, we will discuss in detail the recent works on fundamental understanding how the interfaces and interfacial materials influence the efficiency and stability of HPSCs, and at the same time we show the progress in interfacial design strategies.

2.1. Tuning the Morphology of Perovskite Film by Bottom Interface Engineering

The morphology of the perovskite film, i.e., the grain boundaries and pinholes, plays an important role in the performance and stability of HPSCs. In the early stage of the field, the grain boundaries were thought to create shallow traps benign to the solar cells.[69] Later on, more and more experimental evidences proved the detrimental impact of the grain boundaries in the polycrystalline perovskite film on the performance of HPSCs.[52,70,71] The structural defects or the Schottky defects such as halide vacancies at grain boundaries cause significant first-order recombination, leading to low V_{OC} and severe light soaking effect.[52,70] These grain boundaries facilitate the ion migration, leading to large hysteresis in the current (J)–voltage (V) curves.[72] Moreover, it was also reported that the grain boundaries also form obstacles for the charge transport in perovskite films.[73] The pin holes can form shunt paths by inducing direct contact of the hole and electron transport materials and even causing severe shorts. Grain boundaries and pinholes also form the free path for the penetration of moisture, which induces fast degradation of the device performance.[50,51] Therefore, it is important to grow compact perovskite films with large crystalline grains to achieve efficient and stable HPSCs.

In the past several years, great efforts have been devoted for optimizing the perovskite film morphology and various strategies such as hot casting, solvent annealing, mixed solvents technique, antisolvent dripping, and the interface engineering have been developed.[39,74–76] Among those strategies, the interface engineering of the substrate on which the perovskite film is deposited has shown important successes in the control of the active layer morphology. During the film formation process, the surface energy of the bottom interfacial layers influences the wetting properties of the perovskite solution on the substrate, the crystallization and the morphology of the perovskite by influencing the number of crystallization nuclei, and the spacing between the adjacent nuclei therefore determines the grain size and the grain boundaries of the final perovskite film. The interaction between the terminating group at the surface of the substrate and the perovskite via electrostatic force such as hydrogen bonding or chemical interactions can also influence the crystallization and the perovskite film morphology.

One of the examples of this approach was the use of hydrophobic polymers as bottom HTL. Bi et al. investigated the effects of the wetting and nonwetting surface of the polymer HTL on the grain size of the perovskite film.[76] They demonstrated that the nonwetting surface of the HTL, such as the hydrophobic polymers N4,N4′-bis(4-(6-((3-ethyloxetan-3-yl)methoxy)hexyl)phenyl)-N4,N4′-diphenylbiphenyl-4,4′-diamine (c-OTPD), poly(bis(4-phenyl) (2, 4, 6-trimethylphenyl)amine) (PTAA), and poly (N-9e of the HTL, such as the hydrophobic polymers N4,N4′-bis(4-(6-((3-ethyloxetaniazole)) (PCDTBT) is favorable for forming compact, pin-hole free, and large grains (5 μm on top of PCDTBT) with high aspect ratio due to the reduced number of nuclei, and enlarged spacing in between nuclei by suppressing heterogeneous nucleation and facilitate grain boundary migration using lower drag force (**Figure 4**). In contrast, the wetting surface of the hydrophilic HTLs, such as poly(3,4-ethylenedioxythiophene) polystyrene sulfonate (PEDOT:PSS) and polyvinyl alcohol (PVA), produce much smaller grains (about 300 nm). The perovskite film with enlarged grains obtained on nonwetting HTLs reduced the trap density by 10–100 fold compared to the perovskite film formed on wetting HTLs, which reduced the nonradiative recombination of the charge carriers and improved the charge extraction. As a consequence, all the performance parameters were improved compared to the devices using wetting HTL. Devices using nonwetting HTLs showed PCEs in the range of 17%–18% while devices using PEDOT:PSS did not go higher than 12.3%.[76]

Hydrophobic organic small molecules or 2D materials have also been used as bottom HTLs to grow compact perovskite film with large grains.[77,78] Huang et al., reported a dopant-free HTL, Trux-OMeTAD, which consists of a C3h Truxene-core with arylamine terminals and hexyl side-chains, adopting a planar, rigid, and fully conjugated molecular geometry.[79] These features leads to high hole mobility, hydrophobicity, transparency, and matched frontier energy level with perovskite. Compared to the hydrophilic p-doped spiro-OMeTAD and PEDOT:PSS, compact perovskite films with larger grains form on top of Trux-OMeTAD, reducing the defect density and the charge recombination centers in perovskite films. In addition, the hole injection to, and transport in Trux-OMeTAD are also improved due to its low-lying highest occupied molecular orbit (HOMO) level and fully conjugated molecular geometry. The resulting solar cells showed significant improvement in the PCE (18%) with considerably reduced hysteresis compared to devices based on hydrophilic PEDOT:PSS and spiro-OMeTAD. In 2014, Sun and co-workers for the first time used graphene oxide (GO) to replace PEDOT:PSS as HTL in a p–i–n HPSC.[80] A 2 nm thick GO HTL enabled the formation of homogenous perovskite film with large grains and preferential orientation, which gave rise to devices with a PCE of 12.4%, much higher than the PEDOT:PSS HTL-based cell (average PCE of 9.26%).

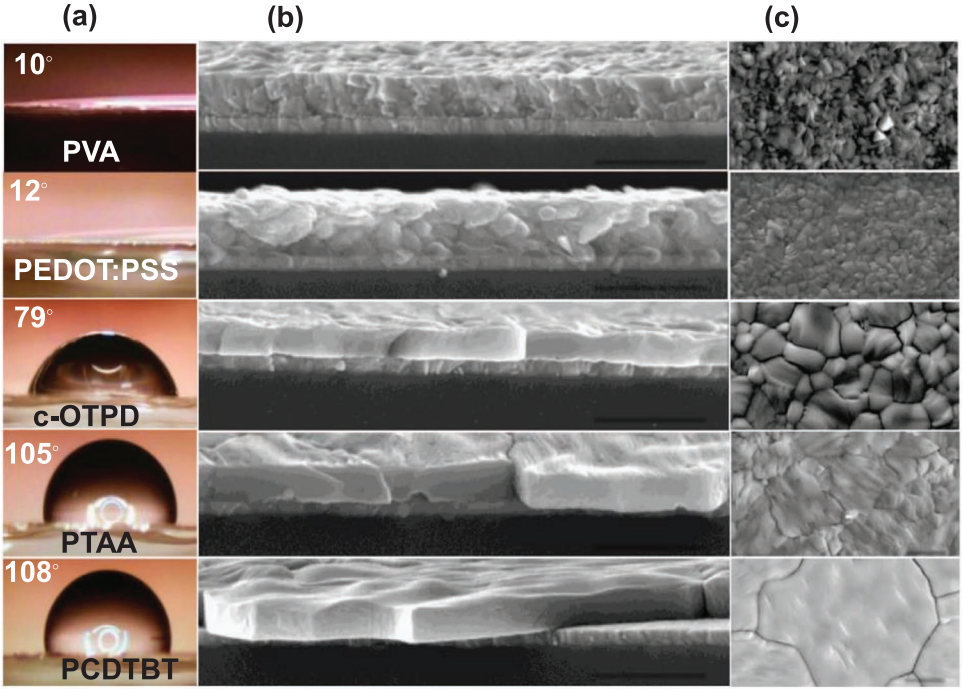

Figure 4. $MAPbI_3$ films grown on wetting and non-wetting HTLs. The contact angle of water on a) the varied HTLs, b) cross-sectional SEM, c) top-view SEM of the $MAPbI_3$ film grown on PVA, PEDOT:PSS, c-OTPD, PTAA, and PCDTBT covered ITO substrates. Scale bars, 1 µm in b,c. Reproduced with permission.[76] Copyright 2015, Nature Publishing Group.

An alternative strategy is to use self-assembled monolayers (SAMs) with terminating groups such as amino or ammonium groups to modify the surface properties of the commonly used inorganic HTL and ETL materials (**Figure 5**). Bai et al. demonstrated that the weak interaction between NiO and perovskite leads to noncompact perovskite film with numerous pinholes and defects, leading to severe charge recombination loss.[81] By modifying the surface of NiO with a diethanolamine SAM, they could increase the interaction of the perovskite and NiO via chemical bonds such as Ni–N and Pb–OH bonds, and produce pin-hole free perovskite film with much lower number of defects (Figure 5a–c). Moreover, the SAM-modified NiO has much deeper VB due to the formation of interfacial dipoles. As a consequence, the device using diethanolamine modified NiO HTL showed considerable improvement in the charge extraction, and more importantly much smaller hysteresis (15.9% at forward sweep and 15.7% at backward sweep) compared to that use bare NiO.

Ogomi et al. inserted HOCO-R-NH_3I monolayer working as an anchor for perovskite ($CH_3NH_3PbI_3$) between the surface of porous metal oxide (titania or alumina) and the perovskite (Figure 5d–f), which improved the PCE of HPSCs from 8% (without HOCO-R-NH_3I monolayer) to 10%.[82] This increase in the efficiency was explained by retardation of charge recombination, and better perovskite crystal growth. Zuo et al. used 3-aminopropanoic acid self-assembled monolayers (C_3-SAM) to modify ZnO electron selective contact (Figure 5g–j).[83] With this method, they successfully obtained compact perovskite film with improved crystallinity and less pin-holes compared to that on pristine ZnO. The improved perovskite morphology was attributed to the improved substrate compatibility with perovskite, where the amino group is expected to change into ammonium by hydrogen ion exchanging and participating into the crystalline structure of perovskite. In addition, the formation of a permanent dipole after surface modification lowers the work function of ZnO and offers better energy level alignment between the perovskite and ZnO, and therefore facilitates the electron extraction. As a result, devices with SAM modified ZnO ETL display a much higher PCE of 14.2% compared to the reference cell (9.8%). Liu et al. inserted a self-assembled silane monolayer between TiO_2 and perovskite. The hydrogen-bonding or electrostatic interactions between the amino groups and the perovskite framework leads to more compact perovskite film with less defects and TiO_2 with lower work function. As a consequence of the suppressed charge recombination, these devices gave much higher performance.[84] Yang et al. performed surface modification of SnO_2 ETL by using 3-aminopropyltriethoxysilane SAMs in planar HPSCs.[85] In this way, they also succeeded in improving the morphology of the $CH_3NH_3PbI_3$ layer, showing increased grain size and uniformity. The resulting device showed a considerable improvement of the PCE from 14.7 to 17.0%. Recently, we employed a pH neutral anionic conjugated polymer (PCP-Na) as HTL and successfully grew compact and pinhole free mixed tin and lead perovskite films.[65]

2.2. Charge Transfer Dynamics at Perovskite/HTM and Perovskite/ETM Interfaces

2.2.1. Energy Alignment at the Interfaces

In order to rationally design efficient and stable HPSCs, it is important to understand the processes occurring at the

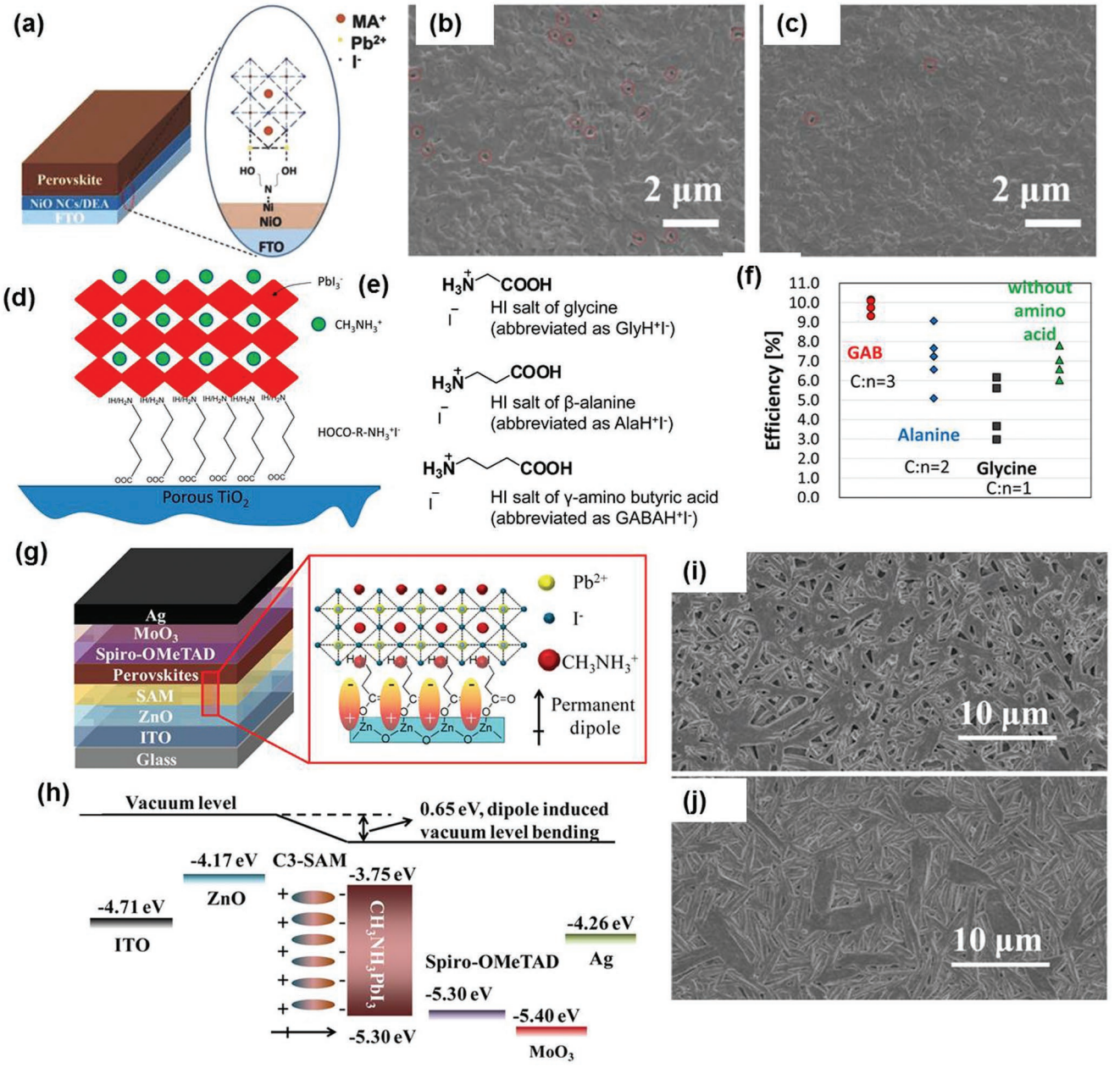

Figure 5. a) Schematic illustration of the surface modification of the NiO NC film with a DEA monolayer, Top-view SEM images b,c) of $CH_3NH_3PbI_{3-x}Cl_x$ films on different substrates. Reproduced with permission.[81] Copyright 2016, Wiley-VCH. d) Schematic illustration of HOCO-R-NH_3I modified titania anode, e) Structure of HOCO-R-$NH_3^+I^-$, f) the PCE of the HPSCs with and without HOCO-R-NH_3I anchor. Reproduced with permission.[82] Copyright 2014, American Chemical Society. Schematic diagram of g) device structure and h) energy level of each layer in HPSCs. i,j) SEM images of perovskite film on different substrates. Reproduced with permission.[83] Copyright 2015, American Chemical Society.

perovskite/HTL (ETL) interface, such as charge transfer/injection and interfacial recombination. The charge transfer process at the perovskite/HTL and perovskite/ETL interfaces is in competition with recombination processes.

Energy-level alignment at those interfaces has been shown to be very critical for the charge transfer dynamics and the charge recombination process, which in turn influences the performance of the solar cells. The absence of energy barrier at the perovskite/interfacial layers facilitates the charge transfer/injection and reduces the charge recombination. Conversely, the energy barrier hinders the charge transfer and leads to strong charge carrier recombination losses.

Impedance spectroscopy measurements revealed energy barriers at the interface between TiO_2 and perovskite, which determines carrier accumulation and significant surface recombination, with consequent reduction in the V_{OC}.[86] Brauer et al. investigated the hole transfer dynamics between a series of HTLs and $MAPbI_3$ by ultrafast transient absorption spectroscopy (TAS).[87] Their results suggested that the hole transfer from photoexcited perovskite to the HTL occurs

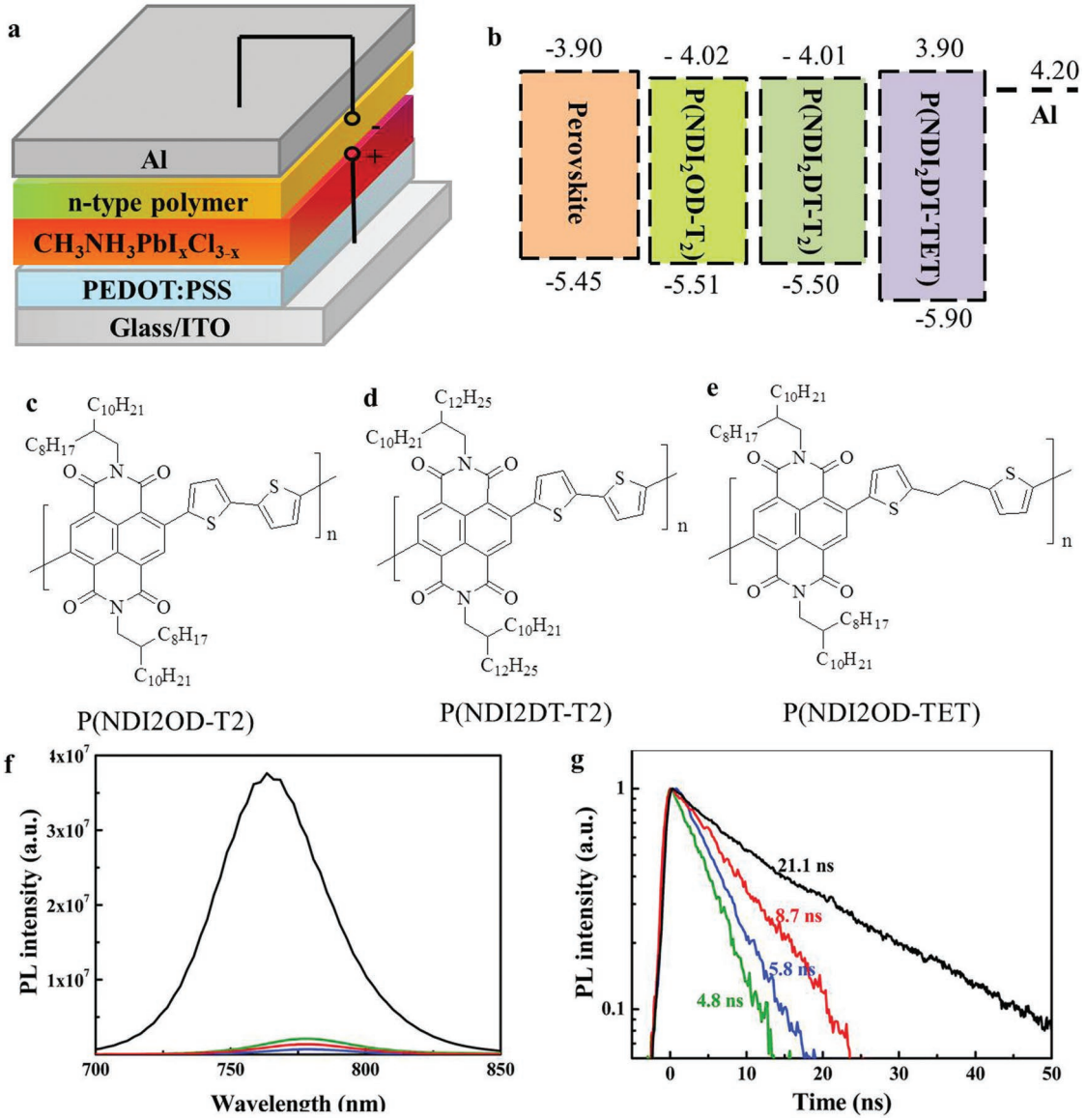

Figure 6. a) Device structure of HPSCs. b) Energy levels of the perovskite and of the three n-type polymers. c,d) The chemical structures of P(NDI2OD-T2, P(NDI2DT-T2), P(NDI2OD-TET), f) Steady state spectra and g) time resolved PL decays for perovskite films without (black line) and with n-type polymer on top (green line for P(NDI2OD-T2), blue line for P(NDI2DT-T2), and red line for P(NDI2OD-TET)). Reproduced with permission.[51] Copyright 2016, The Royal Society of Chemistry.

on a comparable rate (thousands of picoseconds) for P3HT, PCPDTBT, PTAA, which have similar ionization potentials (−5.1, −5.3, and −5.2 eV, respectively) and driving forces for the hole transfer reactions due to similar band-alignment.

In a recent work, we used steady state and time resolved PL measurements to investigate the charge transfer dynamics between three n-type polymers based on naphthalene diimide-bithiophene semiconducting polymers, namely, poly{[*N, N*′-bis(2-octyldodecyl)-naphthalene-1, 4,5, 8-bis(dicarboximide)-2, 6-diyl]-alt-5, 5′-(2, 2′-bithiophene)} (P(NDI2OD-T2)), poly{[N, N′-bis(2-dodecyltetradecyl)-naphthalene-1,4, 5, 8-bis(dicarboximide)-2, 6-diyl]-alt-5, 5′-(2, 2′-bithiophene)}(P(NDI2DT-T2)) and poly{[N, N′-bis(2-octyldodecyl)-1, 4, 5, 8-naphthalenedicarboximide-2, 6-diyl]-alt-5, 5-diyl 2-diyl 2-ethanediyl)bithiophene]} (P(NDI2OD-TET)) (**Figure 6**).[51] Our results showed that all the three n-polymers can quench the PL of the perovskite very efficiently due to matched lowest unoccupied molecular orbitals (LUMO) with the CB of the perovskite and suggested efficient electron transfer from perovskite to those ETLs.

Hutter et al. used TRMC measurements to investigate the charge transfer dynamics between $MAPbI_3$ and organic charge selective transport materials (**Figure 7**a).[26] The fact that the charge transfer process occurs independently of the excitation wavelength and illumination direction (Figure 7b–d) revealed that the charge transfer of electrons or holes to the ETL or HTL is not limited by the charge diffusion in high quality perovskite films ($N_T < 10^{14}$ cm^{-3}) with thicknesses of a few hundred nanometers. The authors found that electron

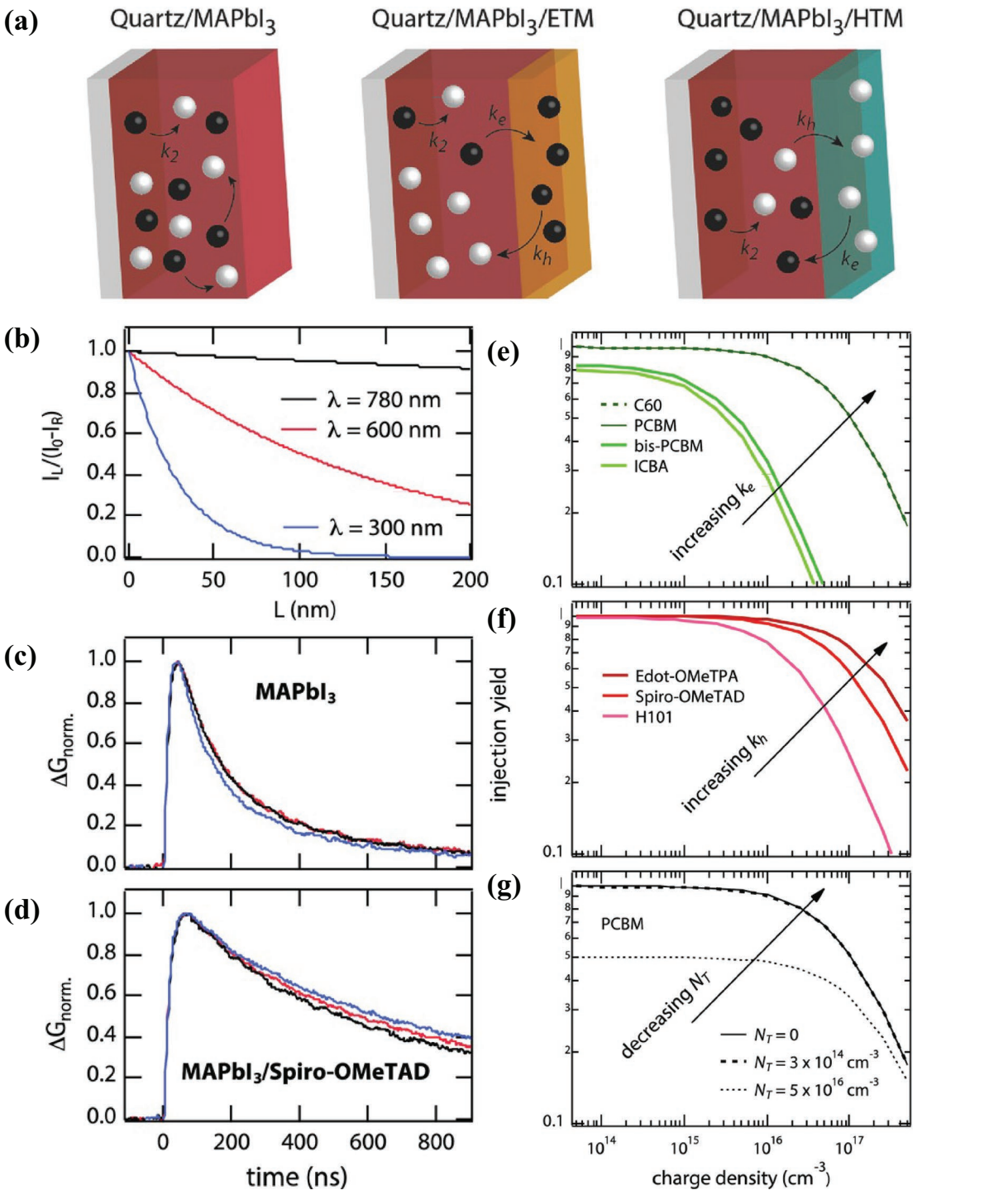

Figure 7. a) Schematic illustration of the perovskite film with and without TL. b) Charge carrier generation profile as function of excitation wavelength, calculated using the experimentally determined absorption coefficients. Normalized time-resolved photoconductance in c) a thin (≈200 nm) $MAPbI_3$ film and d) a bilayer of $MAPbI_3$ and spiro-OMeTAD for a fluence of 1010 cm^{-2} absorbed photons per pulse at excitation wavelengths of 300, 600, and 780 nm. Injection yield as function of charge carrier density for different e) ETLs and f) HTLs. g) Electron transfer yield from $MAPbI_3$ to PCBM as function of the concentration of electron traps (N_T). Reproduced with permission.[26] Copyright 2017, Wiley-VCH.

transfer from $MAPbI_3$ to ICBA or bis-PCBM ETL is one order of magnitude slower compared to the injection of electrons into PCBM or C60 (Figure 7e). This is because the LUMO levels of ICBA and bis-PCBM are 0.2 eV higher than that of PCBM and located above the CB of $MAPbI_3$, losing the driving force for the electron transfer. The hole injection rate at the perovskite/HTL interface also highly depends on the interfacial energy level alignment (Figure 7f). The hole transfer was found to be

much lower at perovskite/H101 interface due to its shallow lying HOMO level (–5.16 eV) compared to the spiro-OMeTAD with HOMO level (–5.21 eV).

A lot of research has been done to optimize the band offsets at HTL/perovskite and ETL/perovskite interfaces to extract the electrons/holes efficiently. The strategies used so far include designing HTL or ETL with suitable HOMO or valence band and LUMO or conduction band, inserting an intermediate layer between either the anode (cathode) and the HTL (ETL) or the HTL (ETL) and the perovskite layer. Furthermore, polar solvent treatment of the HTLs/ETLs, using conjugated polyelectrolyte, and SAMs have been used.[65,88–94] The doping of the perovskite layer is an alternative strategy to manipulate the energy alignment at the perovskite/HTL (ETL), perovskite/anode or perovskite/perovskite interface.[95–97]

Recently, Chen et al. used TPP-OMeTAD and TPP-SMeTAD as HTL in p–i–n HPSCs. The replacement of the oxygen atom (TPP-OMeTAD) on the HTL with sulfur (TPP-SMeTAD) effectively lowers the HOMO of the molecule and offers the stronger Pb–S interaction with perovskites leading to efficient hole injection and surface traps passivation.[88] The TPP-SMeTAD-based p–i–n devices exhibit both improved photovoltaic performance and reduced hysteresis over those based on TPP-OMeTAD. Compared to PEDOT:PSS, the anionic conjugated polymer PCP-Na has higher work function and matches well with the valence band of the mixed tin and lead perovskite films, improving the hole extraction.[65]

Kim et al. used 2D materials such as MoS_2 and WS_2 as HTLs in p–i–n planar HPSCs.[89] The corresponding solar cells using MoS_2 or WS_2 HTLs showed a PCE of 9.53 and 8.02%, respectively. However, Loh and co-workers demonstrated that the hole transfer from the perovskite active layer to the pristine MoS_2 HTL is much less efficient compared to that occurred at the perovskite/sulfur-vacant MoS_2 monolayer interface.[90] This is because the sulfur-vacant MoS_2 has a higher work function of about 5.3 eV, matching better with the valence band of the perovskite layer respect to that of the pristine MoS_2 layer (4.7 eV). Nicholas et al. inserted a thin graphene layer between the TiO_2 ETL and the perovskite layer to form a cascade energy alignment between FTO, TiO_2, and active layer, facilitating the electron collection.[91] Yang et al. inserted a ultrathin graphene quantum dot layer (single-/few-layer) between TiO_2 and the perovskite layer to form a cascade energy alignment at the interfaces, leading to much faster electron transfer (90–106 ps) from perovskite to TiO_2 layer compared to that without graphene quantum dot layer (260–307 ps).[92] Yu et al. used ethanolamine (EA) to treat TiO_2 compact ETM layer, and effectively reduced its work function to 3.7 eV,[93] reducing the energy barrier for electron injection and the bimolecular recombination. In addition, the treatment also passivates the surface traps in perovskite. As discussed earlier, Liu et al. and Zuo et al. successfully reduced the work function of TiO_2 and ZnO by using silane and 3-aminopropanoic acid SAM, facilitating the electron injection.[84,94]

Besides the charge transport layers, doping the perovskite layer is another effective strategy to improve the energy alignment between the active layer and HTLs (ETLs) or electrodes. Qiao et al. demonstrated a gradient heterostructure at the perovskite/ETL and perovskite/HTL interfaces by doping two sides of the perovskite thin films using a "intolerant" n-type heteroatoms (Sb^{3+}, In^{3+}) with mismatched cation sizes and charge states.[95] This gradient band structure facilitates the separation of electrons and holes, and provides continues driving force for the efficient transport and extraction of the charge carriers to the counterpart electrodes. Cui et al. fabricated a p–n homojunction HPSCs by evaporating a p-type perovskite on top of a n-type solution processed perovskite.[96] They claimed that the built-in electric field promotes the charge extraction more effectively. Wu et al. eliminated the energy barrier at the anode/perovskite interface by p-doping the perovskite active layer with a molecular dopant F4TCNQ.[97] As a consequence of the improved charge extraction, the HTL-free HPSC shows an efficiency of about 20%, which is comparable to that obtained using the HTL.

The discussions above assume that the built-in electric field given by the difference in the work functions play a major role in the charge transfer and transport in HPSCs. However, some of the recent studies propose a different scenario, which implies minor role of the electric field instead. Nazeeruddin and co-workers found similar charge transfer time constant no matter if the compact TiO_2 and mesoporous TiO_2 is present or not.[98] Moreover, they found that the V_{OC} of the devices stays relatively constant and is independent of the built-in electric field, the mesoporous morphology, and the difference in work functions across the interfaces. Their results suggested that the V_{OC} is controlled by the splitting of quasi-Fermi levels and recombination inside the perovskite, rather than being governed by the electric field due to the difference in the work functions of the charge transport layers. McGehee et al. systematically tuned the ionization potential of HTLs in inverted device structure, avoiding at the same time any impact to other device parameters by evaporation of a series of HTLs with a wide range of ionization potential.[99] They also found that the photovoltaic performance such as V_{OC} and J_{SC} have a weak dependence on the ionization potentials of the HTLs. Palomares et al. investigated the effects of a series of well-known organic HTLs on the performance of the HPSCs.[100] Their results did not show clear correlation between the HOMO energy levels of the HTLs and the V_{OC}. But they found that the charge transfer from the perovskite to the polymer HTLs (PTB7, P3HT, and PCPDTBT) was slower than to small molecule HTL (Spiro-OMeTAD). Nevertheless, in all these cases, the HOMO level of HTLs was close to or just above the perovskite valence band maximum, or the LUMO level of the ETLs was aligned or slightly below the perovskite conduction band. Bolink and co-workers fabricated a series of fully vacuum-deposited HPSCs with three different HTLs, which allows for the direct substitution of any layer in the device stack with a negligible effect on the other layers.[101] The HTLs including 4,4′, 4″-tris[phenyl(m-tolyl) amino]triphenylamine (m-MTDATA), N4,N4′,N4″,N4‴-tetra([1,1-biphenyl]-4-yl)-[1,1:4,1-terphenyl]-4,4′- diamine (TaTm) and tris(4-carbazoyl-9-ylphenyl)amine (TcTa) have ionization energies of 5.0, 4.4, and 5.7 eV, respectively, leading to a ionization potential difference of 0.66 V. All these HTLs allowed efficient charge extraction though with a large misalignment of the HOMO with the valence band of the perovskite (0.43 eV above or below the perovskite's valence band). Moreover, all the devices produced with these HTLs showed a very small difference in the V_{oc} (60 mV). These results indicate that the

V_{oc} of HPSCs is not limited by the ionization potential of the HTLs. Therefore, future research work should focus on minimizing the interfacial and bulk charge recombination to further improve the V_{OC} of the HPSCs.

2.2.2. Electronic or Ionic Traps at the Interfaces

Other recombination pathways of the charge carriers such as trapping also compete with the charge injection at the interface. If the trapping rate ($\sim k_T N_T$) is higher than the injection rate, the recombination process dominates over injection.[26] For example, only about 50% of the electrons are injected into PCBM when the trap density in perovskite film is up to 5×10^{16} cm^{-3} (Figure 7g).[26]

Previous work from our group and other groups indicate that the trap density in perovskite film is highly dependent on the perovskite film quality.[52,102] Perovskite films with lots of grain boundaries have high trap density and therefore are affected by significant first-order recombination. Conversely, compact perovskite films have much lower trap density and first-order recombination. In the case of high quality films, where the N_T is in the order of 10^{14} cm^{-3}, the trapping rate ($\sim k_T N_T$) is on the order of 10^6 s^{-1} and hence does not impede the charge injection.[26] Therefore, the traps at the perovskite/charge selective interfaces should be removed to enhance the charge transfer. Like any other ionic crystals, the perovskite crystal is prone to form structural defects such as under-coordinated ions at its crystal surface and also at the grain boundaries. Impedance spectroscopy has been extensively investigated to distinguish the electronic and ionic processes occurring either in the film bulk or at the interface between the perovskite film and the charge transport layers in operational cells under one sun illumination.[103–105] Recent experimental studies indicate that the traps at the surface and grain boundaries of the perovskite film dominate the recombination over the bulk traps.[49,86,106] For example, recent impedance studies revealed that the interfacial charge accumulation and recombination mainly occur at the perovskite/ETL interface in the conventional device structure using p-doped spiro-OMeTAD as HTL.[86] Therefore, the choose of the ETL is crucial to the device performance.

Snaith et al. demonstrated that undercoordinated halide ions on the surface of the organic-inorganic halide perovskite crystals could reduce significantly the cell performance by trapping positive charges at the perovskite/HTL interface.[107] They further demonstrated that these exposed iodine ions (hole trapping sites) on the surface of $MAPbI_{3-x}Cl_x$ crystals can be passivated by using the organic molecule iodopentafluorobenzene (IPFB) via supramolecular halogen bonding donor–acceptor complexation (**Figure 8**a,b).[108] As a consequence of the trap passivation, the charge recombination at the perovskite-hole transport material interfaces is suppressed considerably since holes not only survive longer in perovskite film but also transfer to HTL more efficiently (Figure 8c). The HPSCs using IPFB passivated $MAPbI_{3-x}Cl_x$ films showed considerable improvement in the V_{OC} and fill factor (FF) compared to the control devices. In another paper, Snaith et al., demonstrated that the undercoordinated Pb atoms caused by the halide vacancies are electron trap sites, leading to very short charge carrier lifetime and significant charge recombination (Figure 8d-e).[107] Lewis bases such as pyridine and thiophene with lone electron pair were demonstrated to be very efficient passivation agents to fill-in these electron traps, leading to considerable improvement in the charge carrier lifetime and the device performance (Figure 8f). Huang and co-workers demonstrated that PCBM can passivate the electron traps at the surface of perovskite, leading to improved charge transfer at perovskite/PCBM interface.[106] Our recent work showed that PTEG-1 passivates these surface traps more effectively compared to PCBM, and therefore provides more stable and much higher PCE under light illumination.[49]

Besides, the defects at the surface of HTL or ETL also cause charge trapping or accumulation at the perovskite/charge transport material interfaces. Giordano et al. discovered that the electronic trap states at the surface of TiO_2 cause charge accumulation and considerable recombination in the device, leading to low V_{OC} and FF.[54] These traps can be effectively passivated by a simple treatment of the TiO_2 using lithium salts, reducing the charge accumulation at the perovskite/TiO_2 interface and charge recombination. Chen et al. showed that inserting a thin layer of PCBM between TiO_2 and the perovskite film can effectively passivate the interface traps.[109] The femtosecond (fs)-resolved transient absorption spectroscopy performed on working devices allowed to directly compare electron extraction at the TiO_2/perovskite and PCBM/perovskite interface, since the photobleaching (PB) band dynamics follow the electron and hole population dynamics in the hybrid perovskite. A faster decay of the PB band occurs in TiO_2/PCBM-based devices with a lifetime of ≈1.3 ns due to a more efficient charge transfer at PCBM/$MAPbI_3$ interface. Tan et al. demonstrated that chlorine passivates the trap states at the TiO_2 colloidal nanocrystal surface, suppressing the interfacial charge recombination. This strategy produced a high PCE of 19.5% for n-i-p planar device with an area of 1.1 cm^2.[110]

2.3. Charge Transport in HTM and ETM

After the injection of electrons/holes into ETL/HTL, the charge transport capability of these interfacial materials characterized by their conductivity and/or mobility influences the charge extraction and recombination. The low conductivity or mobility of the interfacial materials determines high series resistance, impeding charge carriers to arrive at the electrodes within their lifetime. The consequence is their accumulation at the perovskite/ETL (HTL) interface and their recombination with holes (electrons) in the perovskite active layer, causing significant bimolecular recombination. Our recent work demonstrated that the electron mobility of the n-type polymers dominates the charge collection efficiency in p–i–n HPSCs.[32] The n-type polymers with higher electron mobility, namely P(NDI2OD-T2) and P(NDI2DT-T2) lead to efficient charge collection with negligible bimolecular recombination, while the n-type polymer with lower electron mobility, P(NDI2OD-TET) reduced the charge collection significantly, leading to very low PCE of 1.4%.[51]

For interfacial materials with low intrinsic conductivity or mobility, a common strategy is to n/p-dope them. This doping strategy not only enhances electron/hole transport, but also

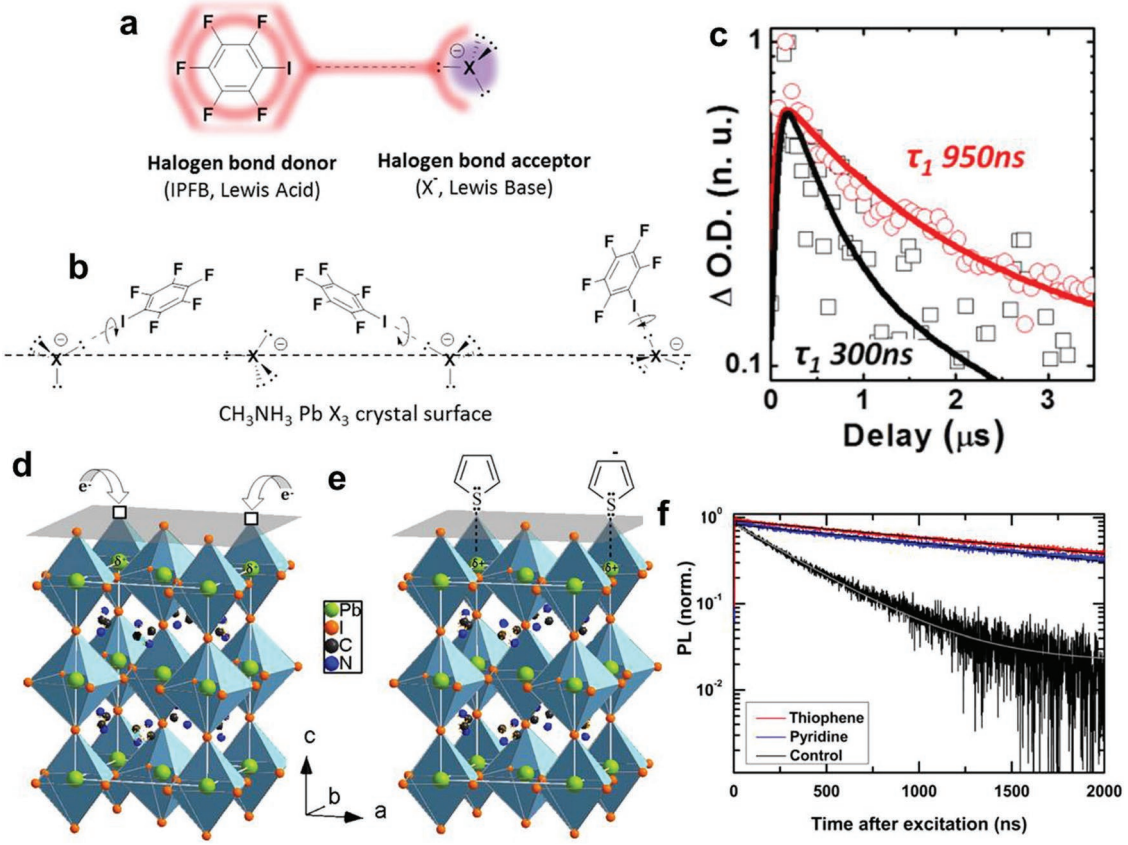

Figure 8. a,b) Schematic view of the halogen bond interaction between the IPFB and a generic halogen anion ($X^- = I^-$, Br^-, Cl^-) with sp^3-hybridized valence electrons. c) Nanosecond transient absorption dynamics for the IPFB treated (circles) and untreated (squares) samples. Reproduced with permission.[108] Copyright 2014, American Chemical Society. d,e) Possible nature of trap sites and proposed passivation mechanism. f) Time-resolved photoluminescence of thiophene- and pyridine-passivated perovskite films as compared to as-prepared films following a 507 nm pulsed excitation (200 kHz, 30 nJ cm^{-2} per pulse). Reproduced with permission.[107] Copyright 2014, American Chemical Society.

modifies the work function of these materials. For organic materials, the n-/p-doping is commonly realized by using molecular dopant, which possess very high HOMO or low LUMO and therefore donate/receive electrons to/from the LUMO/HOMO of the host material. For inorganic materials, the n-dopant or p-dopants go into the crystal lattice or interstitial positions of the host material, and a high temperature processing is necessary in most cases. HTLs or ETLs with high intrinsic electrical conductivity and hole/electron mobility have also been developed. Some of these HTLs or ETLs provide comparable or more efficient charge injection and transport compared to the doped ones.

2.3.1. p-Doping of HTL

In p–i–n device structure, the mostly used organic HTL is the commercially available PEDOT:PSS, which has a conductivity of about 1.6×10^{-3} S cm^{-1}.[111] However, its high hygroscopic and acid nature limits the ambient stability of the HPSCs. In order to address this issue, alternative more water resistant organic or inorganic HTM materials have been developed. Thus far, various inorganic materials such as CuSCN, NiO, CuI, V_2O_5, and PbS have been used as HTLs in the HPSCs.[29,111–114] Of these inorganic HTLs, NiO_x is the most frequently used one in p–i–n HPSCs. The stoichiometric form of NiO is a wide bandgap semiconductor with a very low intrinsic conductivity of 10^{-13} S cm^{-1}. However, the material can be doped by introducing Ni^{3+} acceptors into the NiO crystal lattice. In the conventional sol–gel route, high temperature sintering (≈500 °C) is needed to enhance the crystallinity of NiO. With this method Chen et al., showed NiO with a conductivity of 1.66×10^{-4} S cm^{-1} which is one order of magnitude lower than the one of PEDOT:PSS.[115] The low conductivity of NiO leads to high series resistance (R_s), low charge extraction efficiency, and a low FF for solar cells. Recently, combustion chemistry methods have been reported as a feasible route to prepare highly crystalline solution-processed NiO thin films at much lower temperatures than those used for the traditional sol–gel process.[116]

Substitutional p-doping is an effective way to increase the electrical conductivity of NiO. Several p-dopants for NiO_x such as Li^+, Cu^+, and Cs^+ have been investigated.[115–117] Chen et al. reported Li^+-doped $Ni_xMg_{1-x}O$ films with conductivity of 2.32×10^{-3} S cm^{-1}, which is ≈12 times higher than that of the undoped film (**Figure 9**a).[115] In their case, Mg^{2+} in an amount of 15 mol% was alloyed in the Li^+ doped

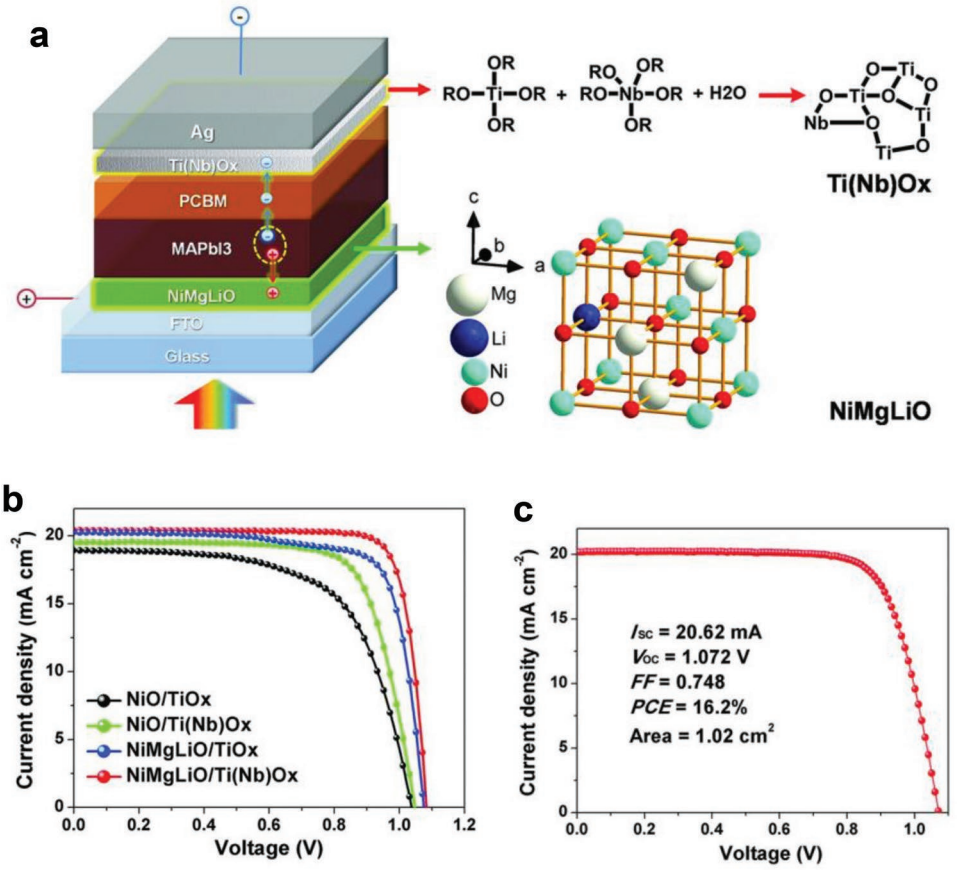

Figure 9. a) Diagram of the cell configuration using the doped charge extraction layers. The right panels show the composition of Ti(Nb)O_x and the crystal structure of Li^+-doped $Ni_xMg_{1-x}O$, denoted as NiMg(Li)O. b) *J–V* curves of solar cells based on different combinations of charge extraction layers. c) *J–V* curve of the best large cell endowed with antireflection film. Reproduced with permission.[115] Copyright 2015, American Association for the Advancement of Science.

NiO film, to compensate for the undesirable positive shift of its VB caused by incorporation of Li^+ into the lattice. The Li^+ content was adjusted to 5 mol%, giving rise to the formula of $Li_{0.05}Mg_{0.15}Ni_{0.8}O$. The resulting dramatic increase in the electrical conductivity enabled 10 to 20 nm thick oxide layers to be used for selective extraction of holes, improving the blocking capability for the electrons, and by reducing the density of pinholes and cracks over large areas. Accordingly, the R_s of the oxides decreased and the shunt resistance (R_{SH}) greatly increased with respect to the undoped layers, leading to a hysteresis free HPSC with FF exceeding 0.8 (Figure 9b). With this strategy, they successfully fabricated large-size (>1 cm^2) HPSCs with an efficiency of up to 16.2% (Figure 9c). Jung et al. reported Cu-doped NiO films (Cu:NiO_x) by both conventional and combustion routes.[118] Compared to the high temperature sol–gel method (500 °C), the latter route produces highly crystalline Cu:NiO_x films with twofold improvement in the conductivity (1.25×10^{-3} S cm^{-1}) at much lower temperature (150 °C). Moreover, it offers better hole extraction/collection capability evidenced by the more efficient PL quenching of the $MAPbI_3$ film respect to the one prepared by conventional sol–gel methods due to its deeper VB. As a result, HPSCs with this low-temperature-processed Cu:NiO_x HTL affords an impressive PCE of 17.74%, outperforming devices based on high-temperature-processed Cu:NiO_x (PCE = 15.52%). Chen et al. developed Cs-doped NiO_x with better electrical conductivity and higher work function.[117] As a consequence, the p–i–n planar HPSCs showed significant improvement in the device performance with a PCE of 19.35% due to the enhanced hole extraction and better band alignment.

In the n–i–p structure HPSCs, triphenylamine (TPA)-based compounds are the most popular small molecules used as HTLs. Among these HTLs, spiro-OMeTAD is the most representative HTM. Due to its intrinsic low conductivity, the solar cells using pure spiro-OMeTAD normally suffers from poor FF due to the very high series resistance, leading to buildup of holes at perovskite/spiro-OMeTAD interface and consequent bimolecular recombination losses.[119,120] To improve its conductivity, p-doping has been performed by exposuring it to oxygen or using p-dopant and additives such as lithium bis(trifluoromethanesulfonyl)imide salt (LiTFSI), 4-*tert*-butylpyridine (TBP) and cobalt (III) complexes.[119,120] The latter strategy has been commonly used due to its advantages of easy and quantitative control of the p-doping level. The same doping strategy has also been successfully applied to other organic HTLs with intrinsic low conductivity including both small molecules and polymers. For example, conjugated polymers, such as P3HT, PCDTBT, PDPPDBTE and poly-(triarylamine) (PTAA), have been p-doped for using as HTL in HPSCs.[121]

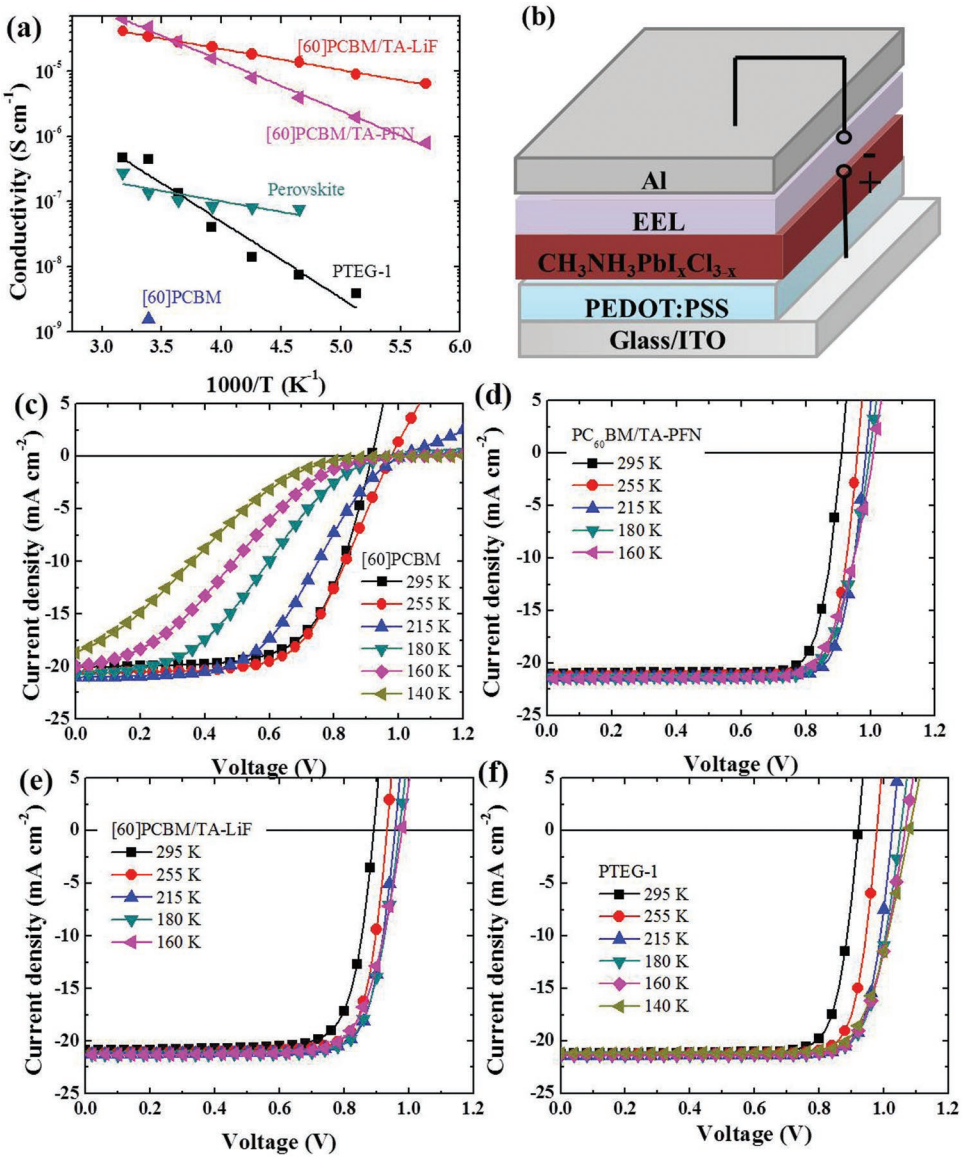

Figure 10. a) Temperature dependence of the conductivity for the perovskite, PCBM, PCBM/TA-LiF, PCBM/TA-PFN, and PTEG-1 samples. b) Schematic of the device structure. Temperature dependence of the *J–V* curves under illumination of the HPSC using c) PCBM, d) PFN-doped PCBM, e) LiF-doped PCBM, and f) PTEG-1 as EEL. Reproduced with permission.[50] Copyright 2017, Wiley-VCH.

2.3.2. n-Doping of ETL

The organic ETLs used in p–i–n HPSCs mainly include fullerene derivatives and n-type polymers.[106,122] Recently, we demonstrated that the charge collection efficiency is highly dependent on the electron transport capability of the ETL materials.[50,51] The commonly used PCBM is not an ideal ETM for HPSCs in terms of its low electrical conductivity (10^{-9} S cm^{-1}) at room temperature (**Figure 10**a).[50] More importantly, the electron transport in PCBM becomes hampered at lower temperature, following the Arrhenius law. As a consequence, electrons cannot escape quickly out of the device and they pile up at the PCBM/perovskite interface and recombine with the holes in the perovskite, leading to strong interfacial recombination of the charge carriers when the temperature is decreased. A pronounced S-shape appears in the *J–V* curves due to the poor charge extraction (Figure 10b,c). By n-doping the PCBM ETL using poly [(9,9-bis(3′-(*N*,*N*-dimethylamino) propyl)-2,7-fluorene)-alt-2,7-(9,9-dioctylfluorene)] (PFN) or LiF, the electrical conductivity of PCBM is enhanced more than three orders of magnitude, leading to enhanced charge extraction over a very broad temperature window (from 295 to 160K) (Figure 10d,e).[101]

When the more conductive PTEG-1 was used to replace PCBM, devices also showed very efficient charge extraction from 295 to 140 K (Figure 10f) similar to devices using n-doped PCBM ETLs. These results demonstrate the critical role of the electron transport capability of ETL in the charge carrier extraction. Also, Bae et al., and Kim et al., doped PCBM with NDMBI for the improvement of HPSCs.[123,124] In 2015,

Li and co-workers improved the electrical conductivity and electron mobility of PCBM layer by incorporating a 2D graphdiyne dopant, which has a delocalized π-systems with sp- and sp^2-hybridized carbon atoms.[125] Accordingly, the solar cells 2D graphdiyne doped PCBM ETL layer displayed higher PCE due to improved charge extraction. Also graphene oxide (GO) has been used to increase the transport of the extraction layer. It is noted that GO is intrinsically an insulator. Sun and co-workers heated this layer at 120 °C to increase its conductivity.[80] To further improve the conductivity, GO has been reduced by different reducing agents such as p-hydrazinobenzenesulfonic acid hemihydrate, and nitrogen.[126,127]

In n–i–p structures, often inorganic materials are used as ETLs, these include TiO_x, ZnO, and SnO_2. Among these ETLs, the most frequently used TiO_x is processed with sol–gel methods giving rise to conductivity in the range of 10^{-8} to 10^{-6} S cm^{-1} due to its amorphous nature.[128] To solve this issue, various n-dopants have also been used to dope TiO_x, such as Nb, Mg, Sn, Li, etc.[54,115,129,130] The n-doping of TiO_x can shift its conduction band edge upwards, passivate its surface electron traps, and improve the electron transport capability, facilitating the electron injection, suppressing the trap assisted recombination, and improving the charge extraction. Using Sn-doped TiO_2 ETL, Zhang et al. improved the J_{SC} and FF significantly.[130] Wang et al. used Mg-doped TiO_2 as ETL, improving the V_{OC} of the HPSCs from 587 to 802 meV.[129]

Despite the high performance achieved in devices using mesoscopic ETL, or compact layers, the high temperature processing becomes a problem for the purpose of commercialization. To overcome this issue, recent studies also paid attention to the low temperature processed ETLs in HPSCs. Tan et al. reported the use of low temperature (150 °C) processed TiO_2 nanoparticles as ETL.[110] Shin et al. developed La-doped $BaSnI_3$ ETL at a temperature of 300 °C, which leads to remarkable improvement in efficiency and stability in a planar device structure compared to that using mesoporous device structures.[131]

2.3.3. HTL with Intrinsic High Conductivity or Mobility

Inorganic or organic HTLs with intrinsic high conductivity or mobility have been reported. Among the inorganic materials, CuI has high work function and conductivity (two orders of magnitude higher than spiro-OMeTAD), and is compatible with perovskite. However, the PCE of the CuI-based solar cells is still very low. Kamat and co-workers employed CuI as hole conducting material, and a PCE of 6.0% was obtained for a HPSC with a structure FTO/compact TiO_2/mesoscopic TiO_2/$CH_3NH_3PbI_3$/CuI/Au.[112] The V_{OC} of the CuI-based device is much lower than that of devices based on spiro-OMeTAD, that is attributed to the higher charge recombination in CuI devices as determined by impedance spectroscopy. Reducing the recombination in these devices may render CuI as a cost-effective HTL in HPSCs. CuSCN is another cheap, abundant p-type semiconductor with high hole mobility, good thermal stability, and suitable work function to match perovskite energy levels. It is intrinsically p-doped and highly transparent over the entire visible and near infrared spectral region. Very recently, Arora et al. demonstrated HPSCs with stabilized efficiency exceeding 20% by using CuSCN HTL formed by fast solvent removal methods as shown in **Figure 11**.[132] Devices using CuSCN HTL exhibit comparable performance to the ones based on spiro-OMeTAD, but display much higher thermal stability. However, the CuSCN-based device has poor operational stability under illumination due to the degradation of the CuSCN/Au contact interface. This issue was simply solved by inserting an interlayer such as the insulating Al_2O_3 or a conductive reduced graphene oxide (rGO), which allowed to retain >95% of the initial device efficiency after 1000 h at 60 °C and maximum power point tracking. These results indicate that CuSCN is a very promising HTL for highly efficient and stable HPSCs.

Dopant-free organic HTL including small molecules, polymers and 2D materials with intrinsic high hole mobility have also been intensively developed. Dopant-free HTLs have the advantage of high hygroscopicity, and can therefore protect the perovskite photoactive layer from exposure to ambient environment, thus enhancing their stability. The dopant-free organic HTLs generally have planar conjugated structures or ordered structures with high symmetry to enhance the carrier delocalization and promote cofacial stacking.

In 2013, Conings et al. reported HPSCs using P3HT as dopant-free HTL with a PCE of 10.8%. In the same year, the same group developed a new conjugated polymer, PCBTDPP as dopant-free HTM in conventional HPSCs, leading to a PCE of 5.55% along with good stability at room temperature in the dark without encapsulation.[133,134] In 2015, Qiao and co-workers reported solution-processed pristine diketopyrrolopyrrole (DPP)-based polymer (PDPP3T) as HTL for HPSCs.[135] The pristine PDPP3T-based HPSCs achieved a PCE of 12.32%, comparable to that (12.34%) using p-doped spiro-OMeTAD based cells. After exposure to air at 40% relative humidity and room temperature, PDPP3T-based cells showed much slower degradation than the spiro-OMeTAD-based cells. The improved stability is ascribed to the high hydrophobicity and hole mobility of pristine PDPP3T HTL. In 2016, Park and co-workers used a random copolymer (RCP) as HTL for HPSCs.[136] This polymer exhibits a deep HOMO energy level (–5.41 eV) and high hole mobility (10^{-3} cm^2 V^{-1} s^{-1}) in the absence of dopants. The RCP-based HPSCs exhibited a PCE as high as 17.3% in the absence of p-dopants. In addition, this device showed dramatically improved ambient stability.

Conjugated small molecular HTLs have the advantages of easy synthesis and purification, tunable energy level, good crystallinity, high mobility and conductivity. To date, dopant-free conjugated small molecule HTLs including planar, linear, and star-shaped molecules have been used in HPSCs.

In 2014, Han and co-workers introduced a pristine tetrathiafulvalene derivative (TTF-1) into HPSCs, giving rise to a PCE of 11.03% and a twofold improvement in ambient stability.[137] Oligothiophenes are a very important class of organic semiconducting materials, which possess high charge carrier density and mobility due to low aromatic and well-defined structures. Tu and co-workers synthesized an "X" swivel-cruciform structure of three 3,3′-bithiophene derivatives (DHPT-SC, DOPT-SC and DEPTSC), which possess better solubility and film-forming properties compared to the linear small molecules because the cross center connection with a single bond could suppress the

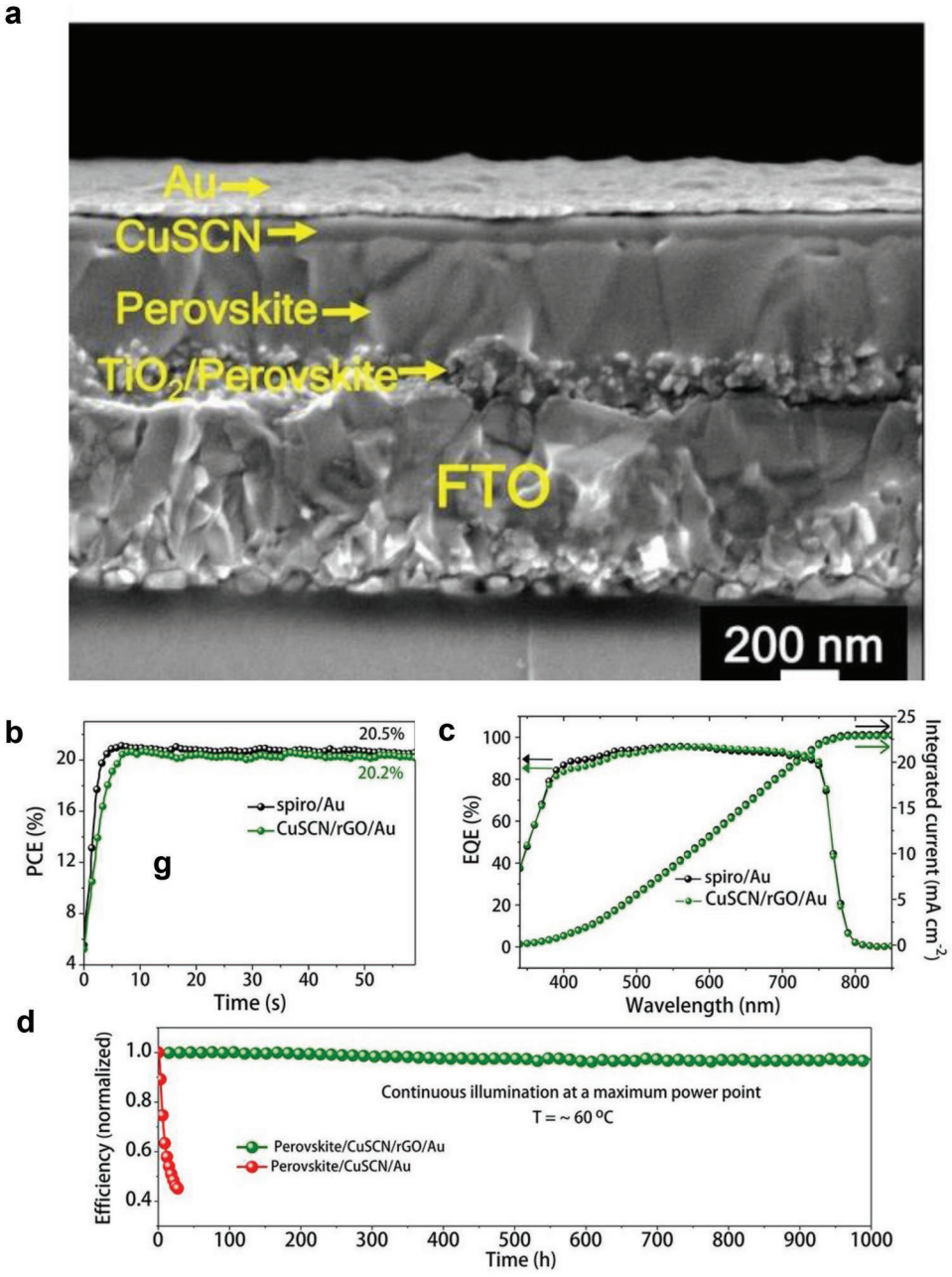

Figure 11. a) Cross-sectional SEM micrograph of the complete device using CuSCN as HTL. b) The maximum power point (MPP) tracking and c) EQE as a function of monochromatic wavelength recorded for spiro-OMeTAD and CuSCN based devices. Reproduced with permission.[132] Copyright 2017, The American Association for the Advancement of Science.

excessive crystallization. HPSCs fabricated using these pristine HTLs have achieved PCEs of 8.35% to 9.73% with good air stability.[138] In 2015, Ahmad and co-workers reported the use of linear acene derivatives as HTLs.[31] TIPS-pentacene has the potential to be a low cost, relatively high hole mobility HTL for perovskite devices. HPSCs based on dopant free TIPS-pentacene HTL yielded a PCE of about 12%. S,N-heteroacenes derivatives combining the favorable properties of oligothiophenes and high charge carrier mobilities of oligoacenes have also been used as dopant-free HTLs in HPSCs.[139,140] In 2014, Gratzel and co-workers. investigated two narrow bandgap oligothiophenes containing S,N-heteropentacene central units. HPSCs using these HTLs achieved a PCE in the range of 9.5%–10.5%.[139] They further reported two S,N-heteropentacene core-based HTLs flanked by an EDOT/thiophene spacer and terminated with dicyanovinylene acceptor units.[140] Mesoscopic HPSCs using these HTMs generated PCE of 10.3–11.4% without any additive or dopant. Sun et al. used a series of electron-rich phenoxazine-unit-based (POZ) A–D–A small molecule HTLs in HPSCs, yielding a promising PCE of 12.8%.[141,142] The high performance of POZ2-based devices employing the electron-deficient benzothiazole as linker was ascribed to its higher hole

mobility and conductivity compared with that of the POZ3 HTL using thiophene as linker. Other types of A–D–A small molecules have also been incorporated as HTLs in HPSCs.[143–145] Liu et al. used two D–A conjugated small molecule consisting of an electron donating dithienosilole (DTS) unit such as an alkylthienyl-substituted benzo[1,2-b:4,5-b′]dithiophene (TBDT) unit (DERDTS–TBDT) and an electron-withdrawing 5,6-difluoro-2,1,3-benzothiadiazole (DFBT) unit for (DORDTS–DFBT), as HTMs in HPSCs, which gave rise to PCE values of 16.2% and 6.2%, respectively.[145] These results should provide guidance for the molecular design of HTLs with intrinsic high charge carrier mobility for highly efficient and stable HPSCs.

The 2D materials are very promising HTLs because of high charge mobility and easy tuning of the fermi levels via functionalization. As discussed in the previously section, MoS_2 and WS_2 have been demonstrated to be very promising HTLs for HPSCs.[89,90]

2.3.4. ETL with Intrinsic High Conductivity or Mobility

Compared to the frequently used TiO_2, ZnO has advantages such as low temperature processing and much higher electron mobility (bulk mobility 205–300 $cm^2\ V^{-1}\ s^{-1}$).[146–148] HPSCs using ZnO nanorods and nanoparticles as ETM showed PCEs of 11.13% and 15.7%, respectively.[149] However, HPSCs using ZnO ETLs suffer from the poor stability due to the chemical reactions occurring at the perovskite/ZnO interface. In this sense, SnO_2 is a more promising ETL with a wider bandgap, high transparency, high electron mobility (bulk mobility: 240 $cm^2\ V^{-1}\ s^{-1}$) and good chemical stability. Low temperature processed SnO_2 has been used in HPSCs. Ke et al. got a PCE of 17.21% for planar HPSCs using SnO_2, which was formed by spin-coating precursor solutions of $SnCl_2.H_2O$ and heating the obtained layer in air at 180 °C.[150] Jiang et al. obtained a certified efficiency of 19.9% with negligible hysteresis by employing solution-processed SnO_2 annealed at 150 °C.[151] Atomic layer deposited (ALD) SnO_2 has also been used in HPSCs.[152] However, SnO_2 ETL made with a combination of spin-coating and chemical bath deposition gave rise to HPSCs of better performance than devices made by ALD. These devices showed a highest efficiency of 21% (planar structure) and lower hysteresis compared to that using TiO_2 ETL.[153] Moreover, these devices retained 82% of the efficiency after aging for 60 h under illumination of 100 $mW\ cm^{-2}$.

Besides the aforementioned inorganic ETLs, the 2D materials such as graphene and its derivatives are also very promising ETLs because of their high charge mobility. Nicholas et al. used a solution-processed nanocomposite of graphene and TiO_2 nanoparticles as compact ETL in mesoscopic HPSCs.[91] Graphene possesses superior electron mobility and also enables the cascade energy alignment from FTO to TiO_2 layer, facilitating the electron collection. As a result, the HPSC using graphene/TiO_2 ETL delivered a much higher PCE of 15.6% compared to TiO_2-based device. In addition, graphene quantum dots were also used as an intermediate layer between mp-TiO_2 and perovskite absorber. The GQDs layer enables faster electron transfer from perovskite to mp-TiO_2 ETL, enhancing the FF and J_{SC} in the corresponding solar cells.[92] Shin and co-workers fabricated a flexible HPSC at a low temperature (<100 °C) by inserting a thin layer of graphene underneath the ZnO QD layer, where the graphene layer not only prevented the direct contact of the perovskite and the HTL with the ITO electrode, but also enhanced electron transport within the device.[154]

2.4. Energy Alignment at ETL/Cathode Interface

The energy alignment at the ETL/cathode interfaces is also a very important factor influencing the charge collection and recombination. The hole/electron injection to the cathode is inhibited in presence of energy barriers, thus increasing the chance of charge recombination loss. To maximize the charge injection at the ETL/cathode interface, the strategy is to remove the energy barriers and form ohmic contacts at those interfaces. To achieve this, various interfacial design strategies have been developed by using transport materials with energy levels that match with the work function of cathode electrodes, inserting another intermediate layer or to form dipoles which are favorable for the charge injection.

Previous studies indicate the presence of the energy barrier and unfavorable band bending at the contact interface between the typical metal cathode electrodes such as Au/Ag/Al and PCBM/C60 ETL interface, which impede the electron injection and extraction.[106,155] To minimize the energy barrier, inorganic metal oxides, low work function metals, metal salts, and organic materials have been reported for interface modification between PCBM and the metal electrode.

In 2013, Snaith et al. inserted a thin compact TiO_2 film between PCBM and the Al electrode, which reduces the energy barrier at the cathode interface and improves the charge collection at the external circuit. In 2015, Chen et al. reported Nb-doped TiO_x as intermediate layer between PCBM and Ag electrode, which brought twofold advantages of high electron transport capability and ohmic contact at the cathode interface.[115] ZnO can also eliminate the energy barrier at the PCBM/Ag interface. You et al. inserted ZnO nanocrystals between the PCBM/Al interface, leading to improved performance with high reproducibility.[156] Zhao et al. improved the electrical conductivity of ZnO by doping it with Al (AZO), which provided suitable energy levels at the cathode interface for electron injection, and higher electron mobility in the ETL.[157] Devices using AZO ETL exhibit an average PCE over 20%. Recently, Zhu et al. eliminated the energy barrier at C_{60}/Ag interface by inserting a layer of SnO_2 NCs.[106] The PCE was demonstrated to be 18.8%, and the device retained over 90% of the initial value after 30 d storage in ambient with >70% relative humidity.

Low work function metals such as Ca, Mg, Ba have also been used to reduce the work function of the Al or Ag electrode.[158] Alkali metal salts such as LiF were demonstrated to effectively eliminate the energy barrier at the cathode interface to facilitate electron extraction in HPSCs, improving the FF and J_{SC} of devices.[35] Several studies indicated that inserting an ultrathin bathocuproine (BCP) layer on top of the thermally evaporated C60 layer can effectively eliminate the energy barrier at C60/Al interface and improve the electron extraction at the cathode interface.[106,159] Moreover, the BCP layer is able to block the holes more effectively due to its deep lying HOMO and

therefore to reduce the leakage current. Shao et al. demonstrated that the device using C60/BCP double ETL layer has considerable hysteresis due to the electron traps at the perovskite film surface.[106] By using a triple layer ETL consisting of PCBM/C60/BCP, they successfully eliminated the hysteresis in the *J–V* curves. Besides, other solution processed fullerene derivatives with hydrophilic functional groups can eliminate the energy barrier at the cathode interface by forming a favorable dipole layer. Liang et al. employed a bis-C60 surfactant as an efficient electron-selective interfacial layer between the PCBM layer and the metal electrode to align the energy levels.[160] Some other fullerene materials were also used to improve the contact between the ETL layer and the top electrode, such as N-methyl-2-(2-perflurooctylphenyl)-3,4-fullero-pyrrolidine (F-C60), an alkylamine group functionalized fullerene complex (DMAPA-C60), tri-alkylamine (C60-N), and [6,6]-phenyl-C61-butyric acid 2-((2-(dimethylamino)ethyl)(methyl)-amino)-ethyl ester (PCBDAN).[114,161,162] Apart from fullerene derivatives, Zhang et al. proposed the use of polyelectrolytes such as polyethylenimine ethoxylated (PEIE) and poly[3-(6-trimethylammoniumhexyl)thiophene] (P3TMAHT) as interlayers on top of PCBM to form an interfacial dipole layer to reduce the work function of the subsequently deposited metal electrode, thereby lowering the electron injection barrier to PCBM.[132]

Li and co-workers proposed titanium isopropoxide (TIPD) as a buffer layer, which showed remarkable ability to improve the charge extraction and suppress charge recombination.[164] Recently, Chen et al. adopted a series of metal acetylacetonates (TiAcac, ZrAcac, and HfAcac) to form double ETLs with PCBM in planar p–i–n device structure.[165] Those metal acetylacetonates were able to effectively reduce interface energy barriers by their dipole and to enhance the electron extraction by forming a barrier-free cathode interface. In 2014, Xue et al. introduced a new amino-functionalized polymer (PN4N) at the PCBM/cathode interface, reducing the contact resistance and suppressing interfacial charge recombination, and leading to an enhancement of PCE from 12.4 to 15.0%.[166]

2.5. Hysteresis in *J–V* Curves

A notorious undesirable phenomenon frequently observed in HPSCs is the hysteresis in the *J–V* curves, which varies depending on the measurement protocol, such as scan direction, rate, voltage range and prebias condition before the measurement.

In 2014, McGehee et al. reported the rate-dependent hysteresis behavior in HPSCs with different device structures.[66] In this work, they showed that the fastest and slowest scans provide hysteresis-free devices, and the intermediate scan speed produces larger hysteresis (**Figure 12**a–d). The preconditioning of the device by applying a bias and exposure to light before the test also influences the device performance. For example, holding the device at a positive bias during light soaking before the test produces higher FF, $J_{SC,}$ and PCE, while holding the device at negative bias gives rise to opposite behavior (Figure 12e,f). The authors argued that the hysteresis effect originates from the polarization in the perovskite active layer because this was observed regardless of the device structure and the charge selective contacts though the magnitude and time constant could be different. Ono et al. reported the temperature dependence of

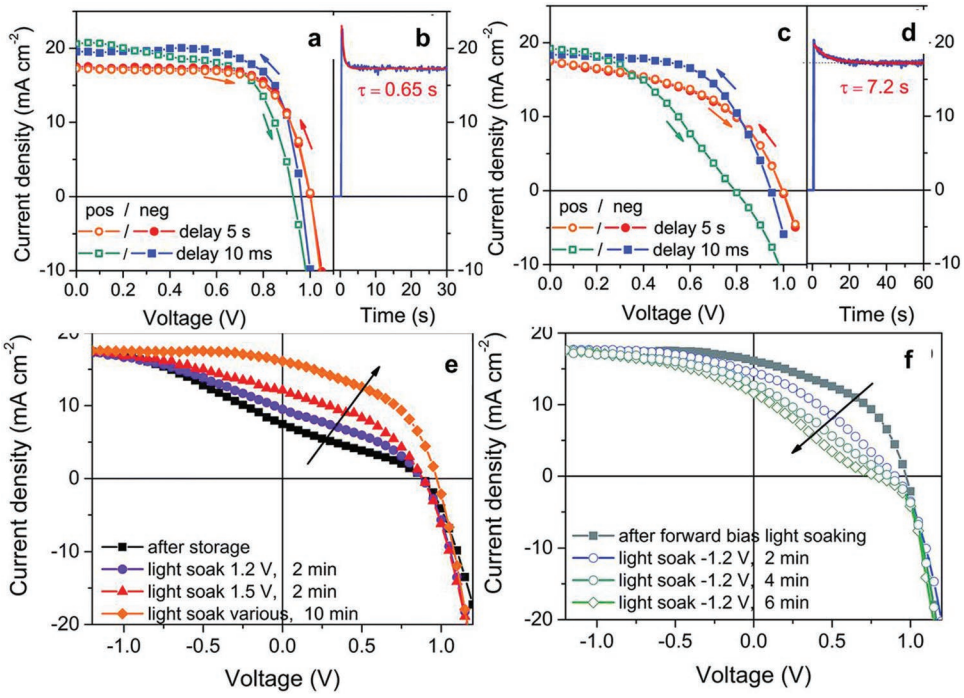

Figure 12. The rate and bias-dependent hysteresis in the *J–V* curves a) mesoporous device structure, c) thin film device structure. b,d) Corresponding short-circuit current transients when switching the devices from V_{OC} to J_{SC} during illumination. Current–voltage measurements at different pre-bias condition of mesoporous-TiO_2 based perovskite-absorber device e) light soaking at negative bias and f) after storage under dark and light soaked at positive bias. Reproduced with permission.[66] Copyright 2014, The Royal Society of Chemistry.

the hysteresis, which is much smaller at 360 K compared to that at 300 and 250 K.[167] The signal cannot be described by a simple monoexponential function, instead multiple charging–discharging processes are responsible for the complex hysteresis behavior. Tress et al. also reported similar rate-dependent hysteresis behavior and preconditioning dependence of the performance of the HPSCs. The electric poling of HPSCs at different biases in dark is able to modulate the efficiency of the HPSCs.[168]

Because the device performance is highly dependent on the measurement protocols, this hysteresis phenomenon caused concerns about the reliability and accuracy in the evaluation of the device performance. Though high efficiency HPSCs have been reported by various independent research groups, it is difficult to make a direct comparison between them due to lack of the standard measurement protocol. Slowing down the scan rate allows to settle the slow transient behavior and therefore produces the most accurate efficiency, however it is difficult to know exactly how slow the scan needs to be performed during the test. These aspects gives extra complication to the question of how to measure the real efficiency of the HPSCs. Currently, it seems to be consensus that the steady-state efficiency tracked at maximum power point voltage is the most reliable performance of HPSCs. However, there are still concerns about the long-term stability of the HPSCs caused by the transient hysteretic behavior. Therefore, it is important to understand the mechanism underlying this effect.

So far, the mechanisms proposed include the ferroelectric properties of perovskite, charge accumulation at the anode/cathode interfaces, the ion migration and charge trapping/detrapping process. Yu and co-workers attributed the hysteresis phenomenon to the ferroelectric effect and built a model based on the ferroelectric diode to explain it.[169] Unger et al. also attributed the transient progress giving rise to the hysteresis to the polarization response of the perovskite, but also proposed that ion migration may also play a role.[66] However, more detailed simulations showed that the MA cations are randomly oriented, and $MAPbI_3$ is not ferroelectric at room temperature.[170] Ono et al. attributed the slow component (in the order of seconds) to the polarization of the perovskite though the underlying reason for the polarization was not explained.[167] Tress et al. proposed the ion migration as the nonelectric reason for the hysteresis based on arguments such as the long time scale of seconds to minutes, ionic nature of the material system, the strong dependence on sweep rate and temperature, the gradual change with the applied voltage not showing any threshold value, and the sensitivity to fabrication and aging. Ions migrate under applied bias and leave the counter charge behind; these ions cannot be extracted and pile up at the interface close to the electrode, screening or increasing the built-in potential depending on the prebias condition, sweep direction, and sweep rate. More recently, many papers came out and attributed the hysteresis to ion migration. Radaelli and co-workers indicated strong frequency dependence of the hysteresis in the range of 0.1 to 150 Hz, with a hysteretic charge density in excess of 1000 μC cm^{-2} at frequencies below 0.4 Hz, a behavior uncharacteristic of ferroelectric response.[171] They found that the observed hysteretic conductance, as well as the presence of a double arc in the impedance spectroscopy, can be fully explained by the migration of mobile ions under bias on a timescale of seconds. Their measurements place an upper limit of ≈1 μC cm^{-2} on any intrinsic frequency-independent polarization, ruling out ferroelectricity as the main cause of current–voltage hysteresis and providing further evidence of the ionic migration in modifying the efficiency of $MAPbI_3$ devices. Indeed, recent studies have shown evidences of the ion migration in perovskite film. Theoretical calculations indicated that halide vacancies have the biggest chance to move due to the small activation energy.[172] Luo et al. directly observed the halide migration in the perovskite single crystal.[173] Yuan et al. observed the migration of the iodide ions under electrical pooling at 330 K.[174] Lee et al. using glow discharge optical emission spectrometry observed the halide migration under small operation bias.[175]

However, the ion migration cannot fully explain why the magnitude of the hysteresis depends on the interfacial contact. In general, planar HPSCs with n–i–p structure using compact TiO_2 ETL and spiro-OMeTAD HTM show more severe hysteresis than the mesoporous TiO_2 scaffold.[66] When the TiO_2 ETL or spiro-OMeTAD HTL is removed from the device structure, the hysteresis becomes even more severe in the case of HTL-free HPSCs.[66] The inverted planar HPSCs with p–i–n device structure using PEDOT:PSS as HTL and with PCBM as ETL typically show much smaller hysteresis than the regular planar device structure.[176] Wu et al. argued that the charge accumulation at the perovskite/ETL interfaces is the reason for the hysteresis.[177] The energy barrier at TiO_2/perovskite interface prevents the charge transfer and leads to pronounced hysteresis in the planar n–i–p devices. The increased TiO_2/perovskite interface helps to improve the charge transfer and produces less pronounced hysteresis in mesoscopic device. The charge extraction at perovskite/PCBM interface is more efficient and produces negligible hysteresis. Simulations by Reenen et al. indicated that the energy barrier at perovskite/charge transport materials influences the magnitude of the hysteresis, but is not the main origin for it.[178]

The charge trapping and detrapping is also proposed to be one of the mechanisms to determine the hysteresis. Shao et al. attributed the traps at the surface and grain boundaries of the perovskite materials to be the origin of the photocurrent hysteresis.[106] Reenen et al. demonstrated that simulations can only reproduce the experimentally observed *J–V* characteristics by combining both the ionic charge and electronic charge trapping at the perovskite/E(H)TL interfaces.[178] Calado et al. observed ion migration regardless of n–i–p and p–i–n device structures with or without significant hysteresis.[176] They combined transient optoelectronic measurements and device simulations and showed that ion migration is similar in both high and low hysteresis $MAPbI_3$ cells. Their simulation results further showed that hysteresis requires the combination of both mobile ionic charge and recombination near the perovskite/charge transport layer interfaces.

Despite the ongoing debate about hysteresis, a clear fact is that the interfacial contacts have great impact on the hysteresis of the HPSCs. Previous studies indicated that the grain boundaries facilitate the ion migration. In Section 2.1, we have discussed how the interfacial contact influences the morphology of the perovskite film and the corresponding hysteresis in the device.

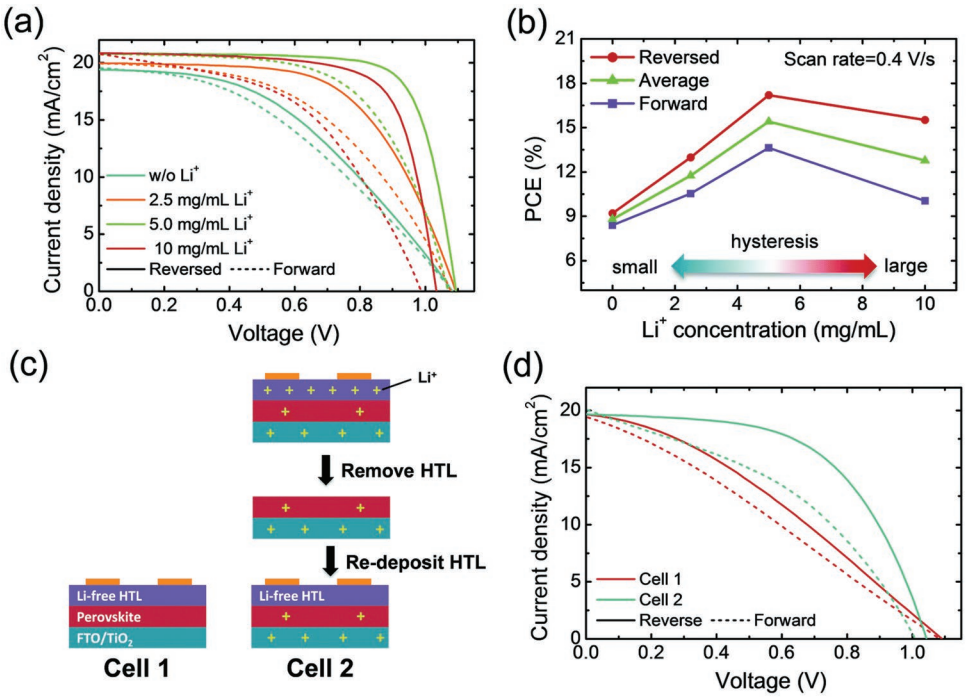

Figure 13. Device performance with different concentration of Li-TFSI in the spiro-OMeTAD HTL. a) *J–V* curves obtained at forward and reverse scan; b) PCE with forward and reverse scan; c) schematics of the solar cell structure; and d) *J–V* curves of solar cells with the same Li-free HTL but different fabrication histories. Reproduced with permission.[184] Copyright 2017, Royal Society of Chemistry.

Here, we discuss more interfacial design strategies to eliminate the hysteresis either by reducing the interfacial traps (both at the surface of the perovskite and of the charge selective materials) or by suppressing the ion migration.

The surface traps at the perovskite film play an important role in the hysteresis. Previous studies have developed various strategies to passivate the trap states at perovskite surface. Shao et al. used PCBM ETL to effectively passivate the traps at the surface of perovskite film and therefore eliminate the hysteresis in the *J–V* curve (**Figure 13**a–c).[106] Zhang et al. treated the as prepared $FAPbI_3$ film with MABr. The excess of MABr on the surface can effectively heal the structure defects at the grain boundaries and suppress the ion migration in the perovskite film.[179] As a consequence of the reduced charge recombination and ion migration, the MABr-treated device showed considerable improvement in the performance with lower hysteresis.

The trap states in the charge transport layers especially in solution processed metal oxides also contribute significantly to the hysteresis. Peng et al. demonstrated that a thin layer of PCBM:PMMA can passivate the defects at or near the perovskite/TiO_2 interface, and thus reduce significantly the interfacial recombination (Figure 13d–f).[180] As a result of the defects passivation, the HPSC showed negligible hysteresis in the *J–V* curve. Woiciechowski et al. used a SAM functionalized C_{60} to modify the top surface of the compact TiO_2 ETL, and reduce the hysteresis significantly compared to that using pristine TiO_2.[181] They attributed this behavior to the passivated electron traps at TiO_2 surface and to the enhanced electron extraction at the interfaces. Giordano et al. showed an alternative effective way to reduce the hysteresis in mesoscopic device structures by doping the TiO_2 scaffold with lithium salt, which improves the charge extraction by passivating the trap states at the surface of TiO_2 and improving its electron mobility.[54] Doping TiO_2 with Zr has the same effects in reducing the hysteresis of the corresponding solar cells.[182] Yang et al. demonstrated that yttrium-doped tin dioxide (Y-SnO_2) ETL significantly reduces the hysteresis and improves the performance of HPSCs compared to the undoped SnO_2.[183] Y-doping not only promoted the formation of well-aligned and more homogeneous distribution of SnO_2 nanosheet arrays (NSAs), but also enlarges the bandgap and upshifted the energy levels, allowing a better perovskite infiltration, contact of perovskite with SnO_2 nanosheets, and energy level alignment, improving the electron transfer from perovskite to ETL and reducing the charge recombination at NSAs/perovskite interfaces.

In addition, the ionic dopants in the interfacial materials also have an effect in the hysteresis of the HPSCs. Very recently, Zhu and co-workers demonstrated that extrinsic ions in the charge selective layer such as (H^+, Li^+ and Na^+) could also migrate across the perovskite layer. The diffusion of Li^+ ions in HPSCs plays an important role in modulating the solar cell performance, tuning TiO_2 carrier-extraction properties, and affecting hysteresis in PSCs (Figure 13).[184] The Li^+ has a high diffusion due to its small ionic radius. In a device structure of TiO_2/perovskite/spiro-OMeTAD, Li^+ ion migration from spiro-OMeTAD to the perovskite and TiO_2 layer was demonstrated by time-of-flight secondary-ion mass spectrometry. Consequently, the cell with higher concentration of Li^+ shows higher hysteresis. Designing the novel charge selective layers with intrinsic high conductivity (dopant-free) or novel dopants without mobile ions is a necessary step to eliminate the hysteresis. So far, plenty of dopant free organic (both small molecules and

polymers) hole transport materials have been developed as discussed in Section 2.3. However, most of the research efforts focused on how the dopant-free charge selective layers influence the PCE and ambient stability, while little attention was addressed to how these dopant-free charge transport layers influence the hysteresis and transient behavior of solar cells.

As described so far, it seems that any efforts that help to increase charge carrier extraction, such as favorable morphology or appropriate interface materials, decreases hysteresis.

2.6. Light Soaking Effect

HPSCs also exhibit light soaking effects under continuous light illumination.[49,52,61] The device performance, and especially the V_{OC} and FF gradually increase under continuous light illumination and eventually reach saturation. This effect is reversible, namely, the performance reverts to the original state when the light illumination is removed. This behavior also causes concern about the instability of the overall output of the HPSCs. Previous studies have attributed the light soaking to either the traps in the bulk and surface of the perovskite film or the ion migration induced polarization in HPSCs.

Stranks et al. found that upon illumination the PL of the $MAPbI_3$ film rises slowly over a time scale of seconds, which matches the rise in the V_{OC} of a complete planar heterojunction HPSC upon illumination with simulated (air mass 1.5 G) sunlight (**Figure 14**a).[61] These results suggest the same underlying mechanism and justifies the relevance of PL studies to better understand perovskite-based solar cells. These slow rises in PL and device performance were attributed to a slow filling and stabilization of the charge trap states by injected or photogenerated electrons, which raises the quasi-Fermi-level for electrons (and hence V_{OC}) and reduces trap mediated nonradiative recombination (Figure 14b). The very slow rise time indicated that the ionic motion may also contribute to the reduction in trap site density over time under illumination or stabilization of the trapped charges.

Hu and co-workers investigated the bulk and interface parameters involved in the light soaking effects and hysteresis phenomena by using capacitance–voltage (C-V), time-dependent photoluminescence (PL), and frequency-dependent capacitance (C-f) measurements for HPSCs with a structure of ITO/PEDOT:PSS/$CH_3NH_3PbI_{3-x}Cl_x$/PCBM/Al (Figure 14c,d).[67] Their results indicated a reduction of the charge accumulation at the electrode interfaces during the light illumination. They proposed two possible reasons for the reduced charge accumulation. First, the photogenerated carriers can neutralize the interfacial defects at the electrode interface upon light illumination. Second, the migration of ions can change the built-in electric field and then affect the charge accumulation at electrode interfaces. These two processes can largely increase the V_{OC} by increasing interfacial potential barrier at electrode interfaces during light illumination. The time-dependent PL and C–f measurements found that the bulk defects within perovskite film are mainly positively charged and can be neutralized by the photogenerated charge carriers, inducing much faster transport of the charge carriers to the respective electrodes and therefore much higher FF.

Xiao et al. reported the switchable photovoltaic phenomenon in HPSCs, which was attributed to the charged ion motion such as MA^+ or iodine vacancies under the applied electrical field.[185] Later Deng et al. reported that in the absence of the applied bias the photovoltage generated by exposing the HPSCs to light illumination can also switch the polarity of the solar cell.[68] When the device is illuminated, the photovoltage acts as an additional bias applied to the device, which breaks the equilibrium state of the device established in dark and starts to pole the perovskite layer. The electric field of photovoltage pointing from PEDOT:PSS to Au electrode drives the positive ions/vacancies to drift toward Au electrode (Figure 14e,f). The accumulated space charges close to Au side cause the n-type doping in that region, and increase the band-bending and thus the built-in voltage as well as the V_{OC} of the devices. The increased V_{OC} further drives the drift of ions/vacancies, forming a positive feedback cycle. Meanwhile, the back diffusion of ions/vacancies also becomes strong once there is significant accumulation of ions, reducing the band-bending. The V_{OC} achieves a maximum when the drift and reverse diffusion of those ions/vacancies is in equilibrium. With almost symmetric work functions of both electrodes, the observed V_{OC} was attributed to the band-bending in the perovskite layer. In this way, positive ions/vacancies accumulated at cathode interface cause n-type doping in the local perovskite material, and the remaining negative space charges cause p-type doping of the perovskite material on the other side, forming a p–i–n or n–i–p homojunction.

Our recent work proposes that the trap states at the surface of the perovskite layer are responsible for the light soaking phenomenon. We demonstrated that both the morphology and the interfacial materials have great influence on light soaking effect in HPSCs (**Figure 15**).[49,52] In the case of noncompact perovskite films, devices using PCBM as ETL display a very severe light soaking effect due to trap-assisted recombination of the charge carriers (Figure 15a–c). At the beginning of the illumination, the device showed very low V_{OC} (0.42 V) and FF (0.46), which increase slowly under illumination reaching saturation (0.87 V and 0.70) after 1.5 h light soaking (Figure 15c). When the device is cooled down, it took much longer time for the device performance to saturate, without reaching the performance achieved at room temperature. This indicated that mobile ions are also contributing to the trap filling process. We proposed that the surface traps are mainly the positively charged iodine vacancies. During the light soaking progress, the photogenerated charge carriers (electrons) and mobile ions (iodine anions) could fill these trap states, leading to increased V_{OC} and FF. Conversely, devices using PTEG-1 ETL showed negligible variation in efficiency before (15.18%) and after light soaking (15.71%) (Figure 15d). PL and impedance measurements indicated that PTEG-1 effectively passivate surface defects on the perovskite film, and reduces considerably trap-assisted recombination. An alternative method to reduce the perovskite films surface traps is to reduce its open grain boundaries and pin holes. When compact perovskite films are used in the same p–i–n device structure, the light soaking effect is minimized due to the reduce number of surface and bulk defects in the film (Figure 15e,f).

As we have shown in Section 2.2.2, Snaith et al. successfully passivated the structural defects, the undercoordinated Pb

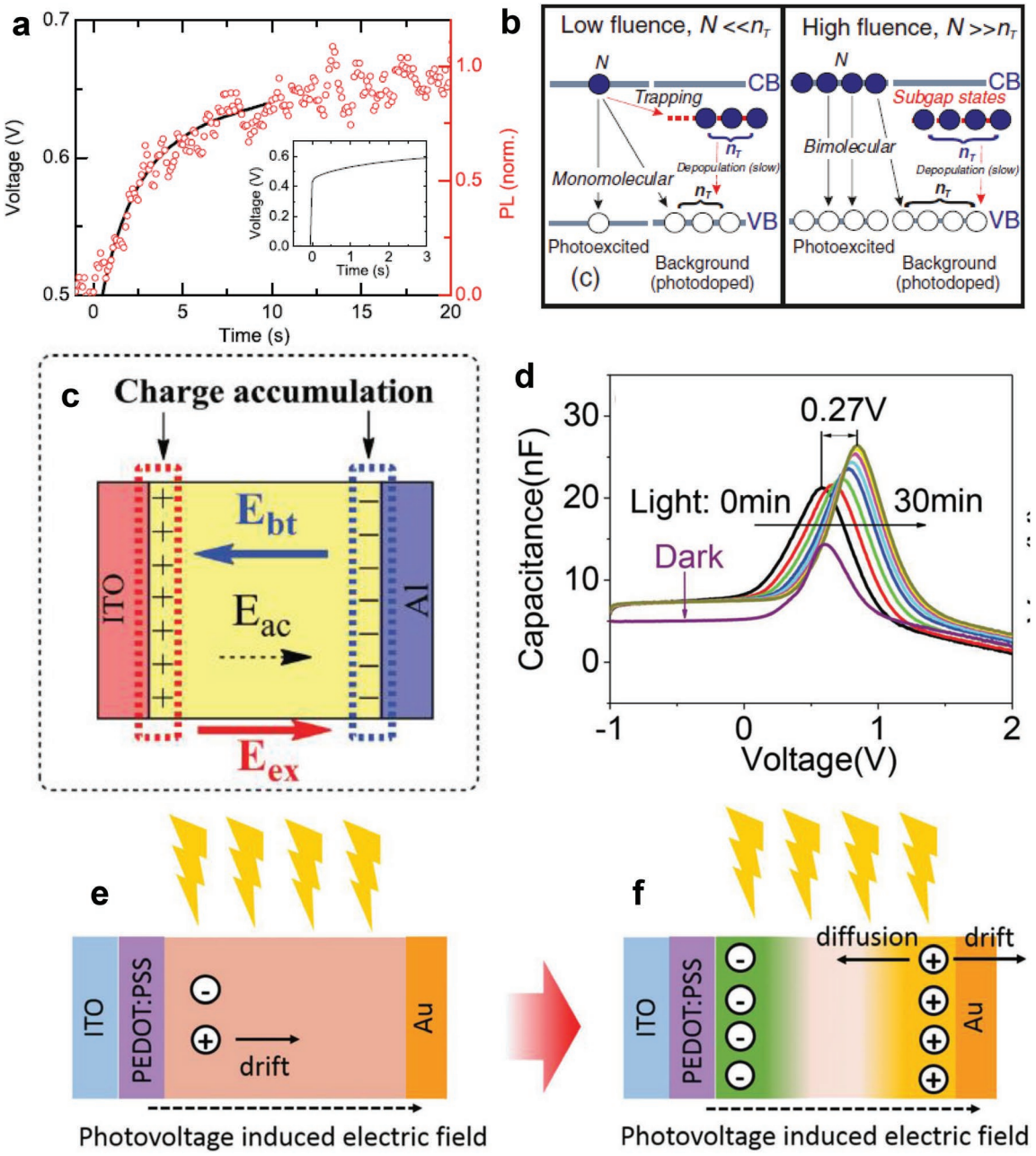

Figure 14. a) V_{OC} increase over time (black line) following illumination of a full device with an intensity approximately equivalent to full sunlight from a white-light LED array source, and PL rise over time (red data) for a flat film photoexcited with an equivalent intensity. b) Schematic to illustrate recombination mechanisms for the low- and high-fluence regimes. Reproduced with permission.[61] Copyright 2014, American Physical Society. c) Schematic diagram to show overall electric field in perovskite solar cells. The effective built-in field E_{bt} consists of the dark field (E_{dark}) and surface accumulation-induced field (E_{ac}). E_{ex} represents an external electric field. d) *C–V* characteristics for ITO/PEDOT:PSS/perovskite/PCBM/Al device under illumination. Reproduced with permission.[67] Copyright 2015, Wiley-VCH. e) Schematic showing the light induced self-pooling process in HPSCs and the energy diagram in perovskite layer a) before and b) after LISP. Reproduced with permission.[68] Copyright 2015, Wiley-VCH.

atoms or halide vacancies, at the surface of $MAPbI_{3-x}Cl_x$ film by using Lewis base such as thiophene and pyridine, reducing significantly the nonradiative electron–hole recombination.[107] The Lewis base passivated device not only has much higher efficiency but also less pronounced light soaking effect compared to the control device.

2.7. Stability

Despite the high efficiency achieved so far, the poor stability of HPSCs under moisture, heat, illumination stresses, caused by the chemical decomposition of the perovskite film or the interfaces can hinder their commercialization.

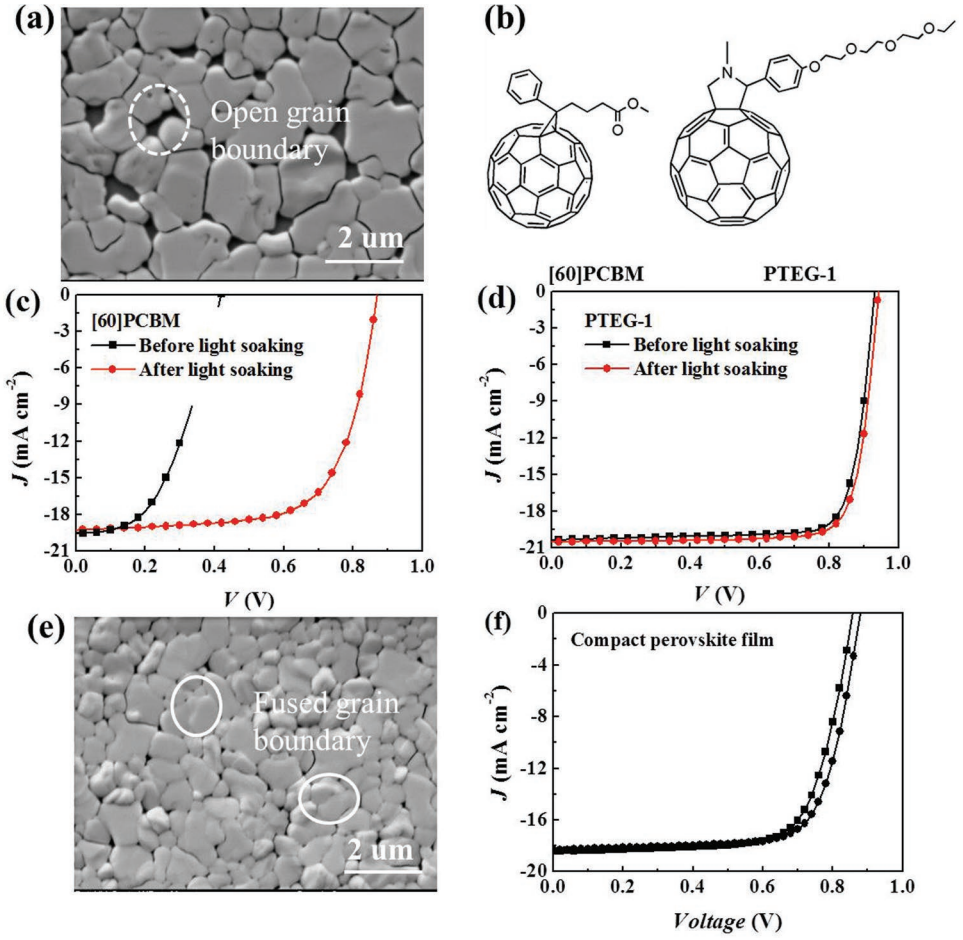

Figure 15. a) SEM image of noncompact perovskite film. Reproduced with permission.[52] Copyright 2016, John Wiley and Sons. b) chemical structures of[60] PCBM and PTEG-1. *J–V* characteristics under illumination of devices using c) PCBM and d) PTEG-1 as ETLs. Reproduced with permission.[49] Copyright 2016, Royal Society of Chemistry. e) SEM image of compact perovskite film. f) *J–V* characteristics under illumination of the device using compact perovskite film and PCBM EEL. Reproduced with permission.[52] Copyright 2016, Wiley-VCH.

As underlined earlier, the perovskite layer, the interfacial layers and their interfaces play a very important role in the stability of HPSCs. In the past several years, great efforts have been devoted to enhance the stability of these devices by tuning the composition of the perovskite film and engineering the interfacial layers. In the sandwich structure, interfacial layers function as protective and sealing shells for the perovskite films, which not only influence the diffusion speed of water but also affects the transit of the decomposed byproducts.

Here we discuss how the interfacial materials and the interfaces influence the stability of the HPSCs, and we review recent advancements in improving the overall device by using various interfacial materials and interface design strategies.

2.7.1. Inhibition of Moisture Induced Degradation

Previous studies indicated that water is prone to cause the chemical decomposition of perovskite films via acid–base reaction. Despite the different decomposition routes proposed, there is consensus that $CH_3NH_3PbI_3$ film decomposes into PbI_2, CH_3NH_3 and I_2 after exposure to moisture.[186,187] The hydrophobicity of the HELs and EELs is very important to slow down the degradation of the perovskite film and therefore to enhance the device stability.

The interfacial materials with low water resistance and high hydrophilicity are therefore not ideal choices for the HPSCs. For example, the frequently used PEDOT:PSS is highly hygroscopic.[188] Therefore, it cannot inhibit the water ingression into perovskite films, leading to HPSCs with poor ambient stability. In contrast, inorganic or hygroscopic organic materials with good moisture resistance as the interfacial layers could significantly improve the ambient stability of HPSCs. NiO is a representative inorganic candidate possessing strong water-blocking capability.

The hygroscopic dopants or polar additives commonly used for the low conductivity interfacial materials such as lithium salt in organic HTMs also cause low ambient stability of HPSCs. As discussed in Section 2.3.4, p-dopant free organic HTMs can block the water molecules more effectively by getting rid of the hydrophilic dopants and considerably

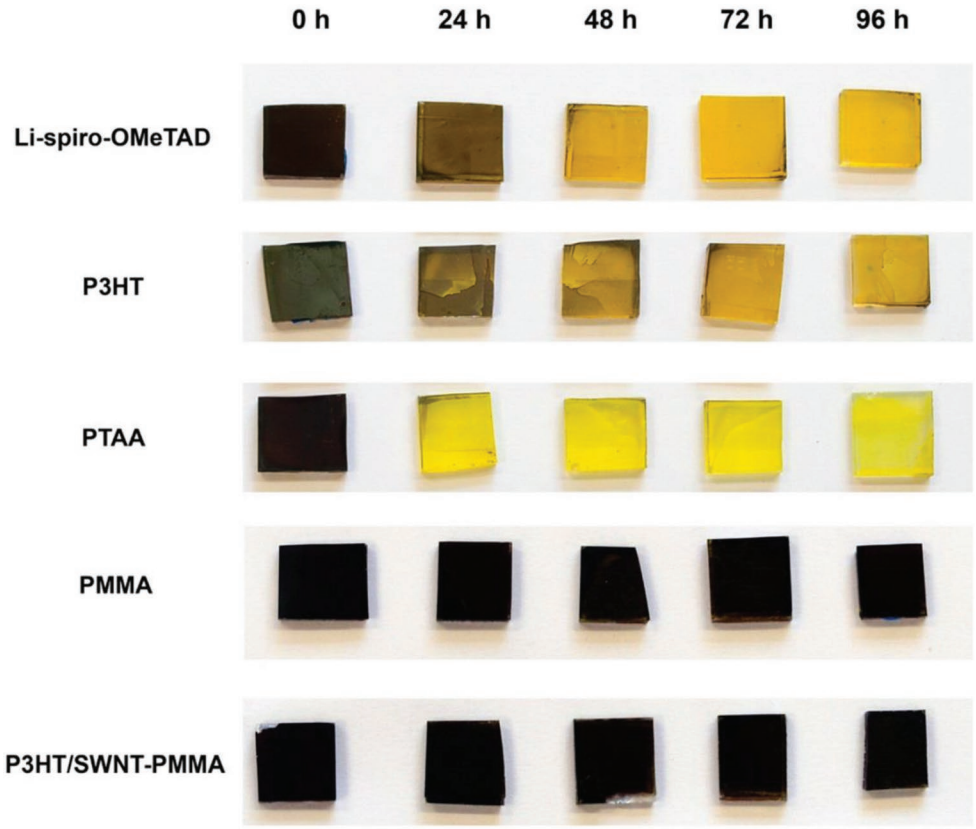

Figure 16. Photo illustrating the visible degradation of the perovskite layer under thermal stress when covered with different organic HTM. Reproduced with permission.[189] Copyright 2014, American Chemical Society.

improve the ambient stability of the HPSCs. Habisreutinger et al. demonstrated that carbon nanotube/polymer composites (P3HT/SWNTs-PMMA) as top HTL can effectively protect the perovskite film from degradation in ambient conditions.[189] The perovskite film with this hydrophobic composite HTL did not show obvious degradation at 80 °C after 96 h in air, while the control film with spiro-OMeTAD, PTAA, and P3HT almost degraded completely under the same condition (**Figure 16**). The 2D materials as HTLs or ETLs have been shown very effective in preventing the penetration of moisture into the perovskite layer. Bao and co-workers demonstrated that a monolayer graphene can protect the perovskite layer from degradation under high temperature and humidity stress due to the impermeability of graphene.[190] The rGO or nitrogen-doped GO as HTL also significantly improve the ambient stability of the HPSCs due to its robustness and resistance to moisture.[126,127] Brabec and co-workers demonstrated that covalently sulfated graphene oxide (oxo-G1) used as the HTL not only enable highly efficient HPSCs, but also improve the stability under various storage conditions.[191] For example, when stored in dark and in ambient environment for 1.900 h, the solar cells using oxo-G1HTL retained 92% of the initial PCE.

Our group and others demonstrated that PCBM is not effective in blocking the moisture penetration due to its hydrophilicity. Bai et al. used a hydrophobic crosslinked silane-modified fullerene layer as ETL and the corresponding solar cells exhibited much higher ambient stability compared to the device using PCBM.[192] By using more hygroscopic n-type polymers as ETL, we improved the ambient stability of the HPSCs considerably.[51] You et al. obtained enhanced ambient stability by using ZnO as ETL and the p-type NiO_x as HTL in a p–i–n device structure.[156] After 60 d storage in air at room temperature, the all-metal-oxide TL devices retained about 90% of their original efficiency, while the control devices using PCBM and PEDOT:PSS underwent a complete degradation after just 5 d.[156] Savva et al. enhanced the device stability of p–i–n HPSCs by inserting AZO between PCBM and Au, which maintained 100% of the initial PCE for over 1000 h of exposure under ISOS-D-1 protocol.[193] Chen et al. demonstrated that inserting metal acetylacetonates (TiAcac, ZrAcac, and HfAcac) on top of PCBM could significantly improve the ambient stability of HPSCs owing to the hydrophobic molecules and the chemically stable metal acetylacetonates.[165]

2.7.2. Preventing Light/Oxygen Induced Degradation

Recent studies indicated that light can induce degradation of the performance of HPSCs. Li et al. found that the UV irradiation causes decomposition of the $MAPbI_3$ film in ultrahigh vacuum, therefore in the absence of oxygen and water.[194] The surface of the perovskite film becomes more n-type and metallic Pb

appears in the XPS spectrum after 120 min UV illumination, indicating the decomposition of the film. The authors argued that the decomposition is a self-limited process because it stops after 480 min when 33% of the total Pb becomes metallic nature.

There are also several reports revealing the effect of light and oxygen on the degradation of $MAPbI_3$ films and the corresponding solar cells at atmospheric pressure. Bryant et al. demonstrated that the synergistic interactions of oxygen and light cause the chemical decomposition of the perovskite, whereas neither oxygen or light alone could initiate the decomposition process (**Figure 17**a).[195] In presence of both light and oxygen, the authors observed degradation products from the aged perovskite film such as superoxide (O_2^-), PbI_2, and

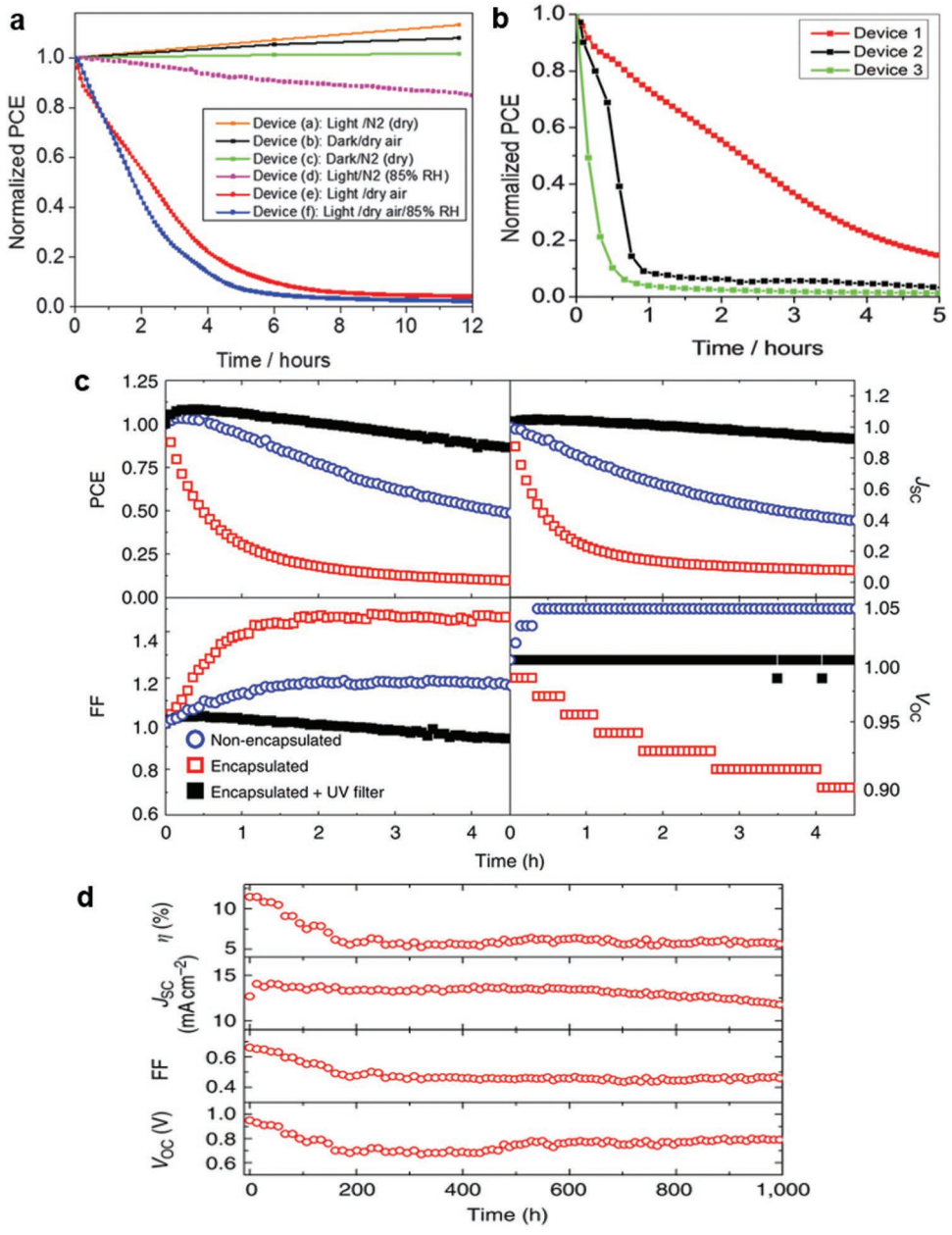

Figure 17. a) Variation with time of the normalized PCE of a FTO/c-TiO_2/ms-TiO_2/$MAPbI_3$/spiro-OMeTAD/Au solar cells stored in different environmental conditions (with dry air comprising 20.95% O_2, 78.09% N_2). b) The normalized PCE versus time for three different devices aged with dry air and light. FTO/c-TiO_2/m-TiO_2/ $MAPbI_3$/spiro-OMeTAD/Au (device 1); FTO/c-TiO_2/$MAPbI_3$/spiro-OMeTAD/Au (device 2) and FTO/c-TiO_2/$MAPbI_3$/spiro-OMeTAD/Au (device 3). Reproduced with permission.[196] Copyright 2013, Springer Nature. c) Evolution of normalized performance parameters over 5 h of AM1.5 100 mW cm^{-2} solar illumination of TiO_2-based HPSCs which are nonencapsulated (blue open circles) and encapsulated with (filled black squares) and without a <435 nm cutoff filter (open red squares). d) Solar cell performance parameters measured directly during aging of a Al_2O_3-based HPSCs under continuous illumination with an intensity of 76.5 mW cm^{-2} at 40 °C. The device was encapsulated with epoxy resin and a glass coverslip in a nitrogen-filled glove box and no UV cutoff filters are used. Reproduced with permission.[197] Copyright 2016, The Royal Society of Chemistry.

I_2. One year later, authors from the same group reported that light and oxygen are the main factors for the low operational stability of $MAPbI_3$-based HPSCs in ambient conditions. In agreement with the previous observation for perovskite films, oxygen or light alone do not cause any obvious degradation in HPSCs. When exposed to both light and dry air, unencapsulated HPSCs degrade on timescales of minutes to a few hours due to the chemical decomposition of the $MAPbI_3$. Such degradation can be slowed down by using interlayers that are able to remove electrons from the perovskite film before their reaction with oxygen. Among the three device structures 1) compact-TiO_2/mesoporous-TiO_2/$MAPbI_3$, 2) compact-TiO_2/$MAPbI_3$, and 3) compact-TiO_2/mesoporous Al_2O_3/$MAPbI_3$, device 1 has the highest photostability due to the improved electron extraction efficiency (Figure 17b). These data demonstrate that the photostability of HPSCs is also critically dependent on the charge transport layers and device configurations.

Snaith et al. also observed light induced degradation in the performance of HPSCs with a mesoporous structure based on a TiO_2 scaffold (Figure 17c).[196] They attributed the degradation to the light induced desorption of the oxygen from TiO_2 surface. They also demonstrated that the use of Al_2O_3 as scaffold effectively improves the photostability of HPSCs (Figure 17d). Researchers from the same group further demonstrated the UV induced chemical decomposition of the perovskite film in n–i–p planar device structure using TiO_2. The decomposition was assigned to the photocatalytic properties of the TiO_2, which is initiated by the defects at the surface of TiO_2. Surface modification of TiO_2 by using a thin layer of CsBr was demonstrated to retard the photocatalytic properties of TiO_2 and eliminate the trap states at TiO_2/perovskite interface, leading to stable perovskite film without chemical degradation after 95 min of UV aging.[197] Fang et al. demonstrated that the light-induced degradation of the 2D perovskite $(PEA)_2PbI_4$, where PEA is 2-phenylethylammonium, starts from the crystal edges and the surface.[198]

2.7.3. Thermal Stability

When operated in practical out-door circumstances, the solar modules are subjected to large variation of temperature. With an ambient temperature of 40 °C, the panel could be heated up to 85 °C, due to continuous sun light strike. Moreover, the deposition of perovskite film itself often involves a thermal treatment temperatures higher than 85 °C, normally 100 °C or even higher. Recent thermogravimetric analysis (TGA) of $MAPbI_3$ revealed that the crystal structure is stable up to 300 °C, but quickly decomposes above this temperature.[199–201] However, degradation of the device performance of HPSCs has been commonly found at much lower temperature. Quan et al. demonstrated that the decomposition starts from the surface of the perovskite film rather than from the bulk because of the greater freedom of the organic molecules to rearrange.[202] Therefore, the organic molecules are key elements to material stability. Using the solid-state nudged elastic band calculations, Fan et al. confirmed that the surface-initiated layer-by-layer degradation path under moderate heating (85 °C) has the lowest energy barrier for crystal transition from tetragonal $MAPbI_3$ to trigonal PbI_2. They further demonstrated that encapsulation of the perovskites with boron nitride flakes suppresses the surface degradation and improve its thermal stability.[203]

Conings et al. demonstrated that the thermal decomposition of the $MAPbI_3$ film in a semifinished structure in the absence of the hole transport layer and the top anode at 85 °C occurs invariably in various atmosphere such as nitrogen, oxygen, and ambient.[204] The calculations from first principle density function theory (DFT) indicate small formation energy (0.11–0.14 eV) for $MAPbI_3$. As the average thermal energy at 85 °C (assuming six degrees of freedom) is 0.093 eV, which is rather close to this formation energy, instabilities of individual unit cells upon annealing at such temperatures, resulting in their decomposition with time can be expected. Experimentally, the decomposition of the perovskite film at 85 °C into PbI_2 was confirmed, and the decomposition rate was found to be dependent on the atmosphere ($N_2 < O_2 <$ ambient air).

Philippe et al. investigated the influence of elevated temperatures on the stability of both $MAPbI_3$ and $MAPbI_{3-x}Cl_x$ films. To do so they used hard X-ray photoelectron spectroscopy to detect the products of the film decomposition.[205] The films were heated in an analysis chamber under ultra-high vacuum to avoid the presence of water and air. Temperatures of 100 °C for 20 min gave rise to a significant reduction of I/Pb, N/Pb ratios indicating the conversion of the perovskite into PbI_2. Further heating till 200 °C caused complete decomposition of the perovskite film into PbI_2. The authors suggest the following reaction for the temperature induced decomposition: $CH_3NH_3PbI_3(s) \rightarrow PbI_2$ (s) + CH_3NH_2 (g) + HI (g). Demonstrating the instability of the perovskite material under elevated temperatures even in absence of water and oxygen.

Kim and co-workers examined the mechanism of the thermal degradation in $MAPbI_3$ perovskite as a function of temperature using in situ surface analysis techniques. They evidenced that the decomposition starts from the surface and progress into the bulk of $MAPbI_3$ films, producing PbI_2 and CH_3NH_3 via an intermediate phase.[206] Obviously, the PCE of $MAPbI_3$-based HPSCs declines significantly at temperatures of ≈85 °C as a result of the decomposition of $MAPbI_3$.

The thermal stability of the HPSCs is also influenced by the interfacial contact and the charge transport layers, in particular by the changes induced in the electrical properties or physical properties upon heating. Park and co-workers observed fast degradation in the performance of the normal device (n–i–p) structure using TiO_2 as ETL and spiro-OMeTAD as HTL upon thermal stress at 85 °C (**Figure 18**a,b).[207] They attributed this thermal instability of HPSCs to the deteriorated hole transport in spiro-OMeTAD layer due to its low glass phase transition temperature. This conclusion was further confirmed by the fact that the device performance recovered when the degraded spiro-OMeTAD layer was replaced with a fresh one (Figure 18c).[178] The inverted device structure using NiO_x as HTL and PCBM as ETL has much higher thermal stability. Therefore, in order to improve the thermal stability of the HPSCs, HTL and ETL of thermally stable structural and electrical properties should be developed.

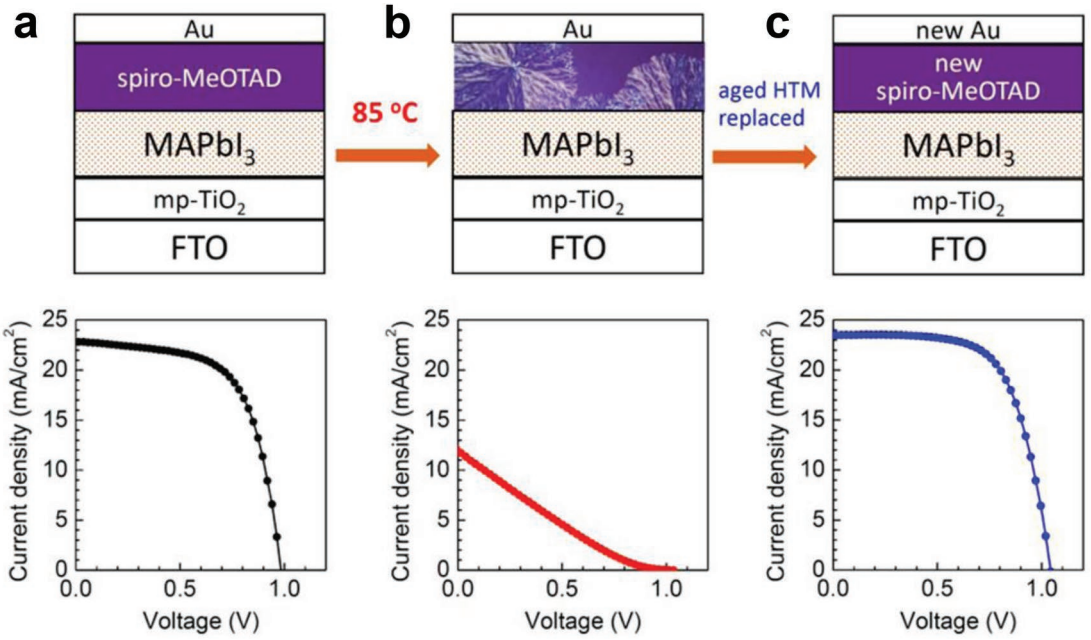

Figure 18. a) Fresh device, b) aged device at 85 °C, c) The aged device with fresh HTL and Au electrode and their corresponding *J–V* curves under one sun illumination. Reproduced with permission.[207] Copyright 2017, American Chemical Society.

Heat also initiates the chemical decomposition of the perovskite film when in contact with an interfacial materials of basic nature. Hu et al. observed the decomposition of the $MAPbI_3$ films upon heating to 80 °C for 1 h caused by the basic nature of ZnO. The unencapsulated HPSCs containing ZnO ETL degraded faster than those prepared without the ZnO layer, highlighting its deleterious impact on the thermal stability of the device. The replacement ZnO with Cs_2CO_3 was the strategy used to considerably improve the thermal stability of the perovskite film and the corresponding solar cells. Kelly and coworkers showed that the basic nature of the ZnO surface leads to proton-transfer reactions at the ZnO/$CH_3NH_3PbI_3$ interface, resulting in decomposition of the perovskite film.[208] The presence of hydroxyl groups and/or residual acetate ligands at the surface of ZnO can accelerate the decomposition process, while the calcination of the ZnO layer results in a more thermally stable ZnO/$CH_3NH_3PbI_3$ interface due to removal of hydroxyl groups, albeit at the cost of a small decrease in PCE. An intermediate layer should be adopted to avoid the direct contact of ZnO with perovskite film to improve the thermal stability of the solar cells using ZnO as ETL. Fan et al. employed a quasi-core shell structure composed of ZnO and reduced graphene oxide (rGO) quantum dots as ETL.[209] The rGO shell not only passivates the surface of ZnO, but also helps to extract the charge carriers quickly from the perovskite layer reducing the carrier recombination. The HPSCs based on ZnO/rGO layer displayed a superior PCE of 15.2% compared to that based on pristine ZnO under AM1.5G illumination. More importantly, the core–shell ETL structure offers much higher ambient stability compared to that using ZnO due to the suppressed reaction path between perovskite and ZnO. The efficiency of devices using core–shell ETL lost only 10% efficiency after 30 d in ambient air compared to the 90% decay in efficiency of devices using pristine ZnO ETL.

Heat was also reported to cause migration of metal atoms into perovskite films, leading to the degradation of the HPSCs. Domanski et al. demonstrated that by heating the device employing a spiro-OMeTAD/Au (Ag) back contact at $T > 80$ °C causes irreversible degradation to the device performance.[210] Through elemental analysis on aged devices, they observed considerable amounts of Au near TiO_2/SnO_2 interface, indicating diffusion of Au across the HTL into the perovskite layer. They proved that the diffusion of Au into perovskite film is the main factor to cause the irreversible loss in V_{OC}, FF, and J_{SC} in the aged devices, because the solar cell with the same heat stress performed after the removal of the Au top electrode kept almost the same efficiency when fresh gold was deposited. Therefore, gold causes not only shunts but also creates trap states in perovskite film and thus cause significant charge recombination and loss in the performance.

2.7.4. Preventing the Electrodes from Corrosion

The corrosion of the active electrodes typically Ag and Al by either the mobile halides in the perovskite film or the decomposed byproduct such as volatile I_2 and HI has also become a serious problem for the operation of the HPSCs.[211,212] In this case, the device performance drops because insulating products such as AgI prevent the charge extraction and increase the charge recombination. Unlike the degradation caused by external contaminants, the corrosion of the electrode appears to be unavoidable, and cannot be solved simply by encapsulation.

It has been reported that Ag gets corroded when in contact with perovskite films suggesting the formation of insulating AgI as the reason for the decay in the device performance.[213] Recently, Cheng and co-workers studied stability of encapsulated, planar-structured $MAPbI_3$ with an Ag back-contact electrode layer at elevated temperature and humidity.[214] They observed diffraction peaks assigned to PbI_2 and AgI peaks

when the samples were kept at 55 °C, 50% humidity for 500 h.

Though the interfacial layers avoid the direct contact of perovskite film with metal electrodes, the inherent mobile halide ions in perovskite film can easily diffuse across the interfacial materials to react with the metal electrodes due to the very small activation energy for their migration. Back et al. demonstrated that the corrosion of the electrodes (Ag and Al) by the iodine anions is a main factor to cause the device degradation in nitrogen atmosphere (**Figure 19**a–c).[215] They developed a chemical inhibition layer (CIL) by inserting an amine-decorated TiO_x (AM-TiO_x) layer between PCBM and Al or Ag and succeeded in chemically neutralizing/freezing these ionic defects through ionic (N^+–I^-) interaction (Figure 19d–f). In this way, the corrosion of the electrodes was almost completely suppressed. As a consequence, the device with CIL showed much better stability both in nitrogen atmosphere and in ambient air compared to the control device without CIL.

Similar to other extrinsic factors, the light induced decomposition of the perovskite also causes corrosion of the electrode due to the diffusion of the ions and the volatile species, leading to significant degradation in the device performance. Yang et al. demonstrated that the reactivity of the perovskite with the cathode contact is the major degradation pathway in inverted planar devices of the type ITO/PEDOT:PSS/ $MAPbI_3$/PCBM/metal, where the cathode metal are varied from Al, Ag, Ca, and Cr_2O_3/Cr.[212] During 4 h illumination of the above devices in a nitrogen filled glove box, all the devices show a sharp decrease in the device performance due to the corrosion of the metal electrodes.

3. Conclusions and Outlook

In this paper, we have discussed the role of the charge selective contacts and their interfaces in the operation and performance of HPSCs and provided an overview of the recent progress in interfacial design strategies toward highly efficient and stable HPSCs. Though the record efficiency of the lab scale HPSCs is 25.2%, the efficiency of the solar modules is much lower, and the increased dimension of the solar cells not only increases the contact series resistance but also poses challenges for the formation of uniform layers. At the moment the lifetime of the HPSCs is still too short to meet the commercial standard of 25 years. Moreover, we believe that there is still plenty of room to improve the PCE and specially to increase the stability of HPSCs, which highly depends on the delicate design of the interfaces and the interfacial materials. Intense and intimate collaborations between physicist and chemists is necessary to overcome the great challenge to design such ideal interfaces and materials for highly stable and efficient solar cells, which should satisfy the following criteria: 1) suitable surface energy for growth of the compact perovskite film with large grains; 2) proper energy-level alignment between adjacent layers to reduce the energy barrier for charge transfer and injection; 3) high charge extraction and transport capacity; 4) low temperature solution processing and good film forming properties to form compact and pin hole free interfacial layers; 5) no chemical reactivity with the perovskite film; 6) good passivation capabilities to reduce the trap states in perovskite film; 7) high resistance to moisture penetration; and 8) protection of the metal electrode from migrating iodide ions.

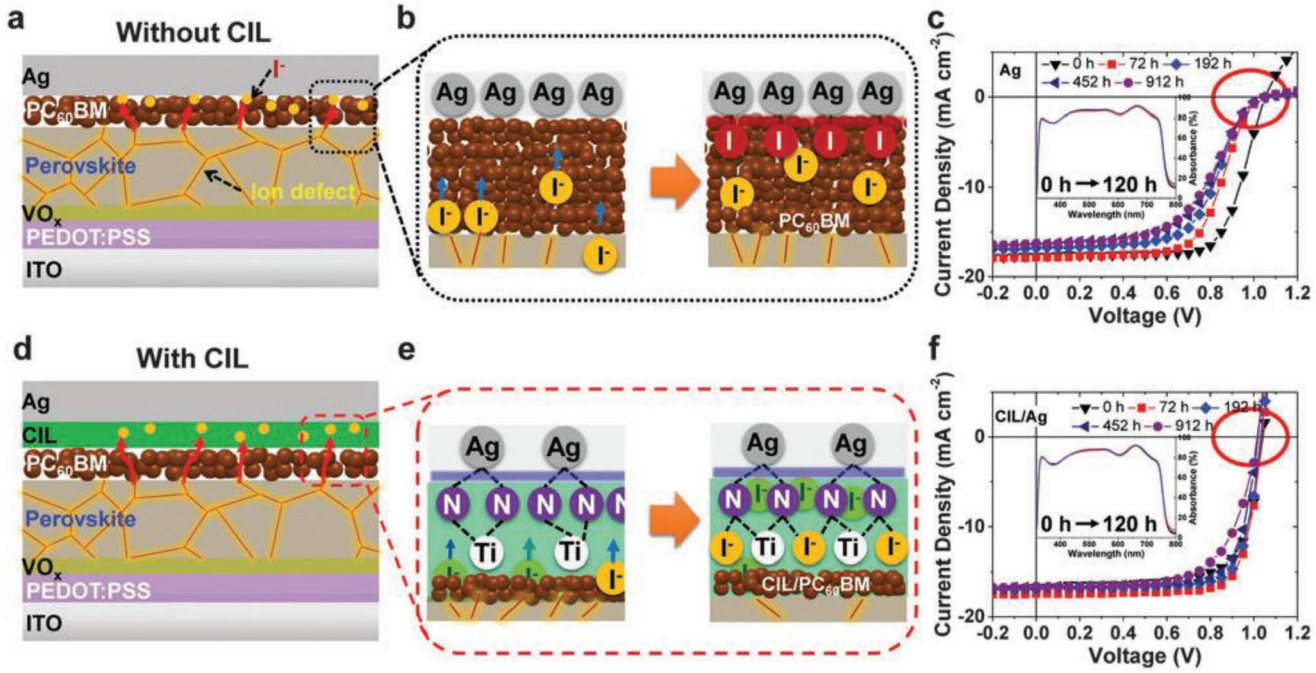

Figure 19. a,b) The reference structure of p–i–n HPSCs and the cathode degradation process. c) Variation of *J*–*V* characteristics of the reference cell and absorption spectra (inset) with aging time in nitrogen atmosphere. d,e) The p–i–n HPSCs with a chemical inhibition layer and cathode protection process, f) *J*–*V* characteristics of the device with chemical inhibition layer and absorption spectra (inset). Reproduced with permission.[215] Copyright 2016, The Royal Society of Chemistry.

Acknowledgements

The authors would like to thank A. F. Kamp for his technical support. This article is part of the *Advanced Materials Interfaces* Hall of Fame article series, which highlights the work of top interface and surface scientists.

Conflict of Interest

The authors declare no conflict of interest.

Keywords

charge recombination, charge transport layer, interface, perovskite solar cells, stability

Received: August 23, 2019
Revised: October 6, 2019
Published online:

[1] Y. Hu, Z. Zhang, A. Mei, Y. Jiang, X. Hou, Q. Wang, K. Du, Y. Rong, Y. Zhou, G. Xu, H. Han, *Adv. Mater.* **2018**, *30*, 1705786.
[2] M. A. Green, A. Ho-Baillie, H. J. Snaith, *Nat. Photonics* **2014**, *8*, 506.
[3] S. Shao, J. Liu, G. Portale, H.-H. Fang, G. R. Blake, G. H. ten Brink, L. J. A. Koster, M. A. Loi, *Adv. Energy Mater.* **2018**, *8*, 1702019.
[4] N.-G. Park, *Mater. Today* **2015**, *18*, 65.
[5] G. Xing, N. Mathews, S. Sun, S. S. Lim, Y. M. Lam, M. Grätzel, S. Mhaisalkar, T. C. Sum, *Science* **2013**, *342*, 344.
[6] D. Shi, V. Adinolfi, R. Comin, M. Yuan, E. Alarousu, A. Buin, Y. Chen, S. Hoogland, A. Rothenberger, K. Katsiev, Y. Losovyj, X. Zhang, P. A. Dowben, O. F. Mohammed, E. H. Sargent, O. M. Bakr, *Science* **2015**, *347*, 519.
[7] S. D. Stranks, G. E. Eperon, G. Grancini, C. Menelaou, M. J. P. Alcocer, T. Leijtens, L. M. Herz, A. Petrozza, H. J. Snaith, *Science* **2013**, *342*, 341.
[8] L. M. Herz, *ACS Energy Lett.* **2017**, *2*, 1539.
[9] A. Miyata, A. Mitioglu, P. Plochocka, O. Portugall, J. T.-W. Wang, S. D. Stranks, H. J. Snaith, R. J. Nicholas, *Nat. Phys.* **2015**, *11*, 582.
[10] J. Even, L. Pedesseau, C. Katan, *J. Phys. Chem. C* **2014**, *118*, 11566.
[11] M. Hirasawa, T. Ishihara, T. Goto, K. Uchida, N. Miura, *Phys. B* **1994**, *201*, 427.
[12] K. Tanaka, T. Takahashi, T. Ban, T. Kondo, K. Uchida, N. Miura, *Solid State Commun.* **2003**, *127*, 619.
[13] Y. Deng, E. Peng, Y. Shao, Z. Xiao, Q. Dong, J. Huang, *Energy Environ. Sci.* **2015**, *8*, 1544.
[14] K. Hwang, Y.-S. Jung, Y.-J. Heo, F. H. Scholes, S. E. Watkins, J. Subbiah, D. J. Jones, D.-Y. Kim, D. Vak, *Adv. Mater.* **2015**, *27*, 1241.
[15] S. Razza, S. Castro-Hermosa, A. Di Carlo, T. M. Brown, *APL Mater.* **2016**, *4*, 091508.
[16] J. M. Ball, S. D. Stranks, M. T. Hörantner, S. Hüttner, W. Zhang, E. J. W. Crossland, I. Ramirez, M. Riede, M. B. Johnston, R. H. Friend, H. J. Snaith, *Energy Environ. Sci.* **2015**, *8*, 602.
[17] A. Kojima, K. Teshima, Y. Shirai, T. Miyasaka, *J. Am. Chem. Soc.* **2009**, *131*, 6050.
[18] H.-S. Kim, C.-R. Lee, J.-H. Im, K.-B. Lee, T. Moehl, A. Marchioro, S.-J. Moon, R. Humphry-Baker, J.-H. Yum, J. E. Moser, M. Grätzel, N.-G. Park, *Sci. Rep.* **2012**, *2*, 591.
[19] M. M. Lee, J. Teuscher, T. Miyasaka, T. N. Murakami, H. J. Snaith, *Science* **2012**, *338*, 643.
[20] L. Etgar, P. Gao, Z. Xue, Q. Peng, A. K. Chandiran, B. Liu, M. K. Nazeeruddin, M. Grätzel, *J. Am. Chem. Soc.* **2012**, *134*, 17396.
[21] D. Liu, J. Yang, T. L. Kelly, *J. Am. Chem. Soc.* **2014**, *136*, 17116.
[22] J. M. Ball, M. M. Lee, A. Hey, H. J. Snaith, *Energy Environ. Sci.* **2013**, *6*, 1739.
[23] J.-Y. Jeng, Y.-F. Chiang, M.-H. Lee, S.-R. Peng, T.-F. Guo, P. Chen, T.-C. Wen, *Adv. Mater.* **2013**, *25*, 3727.
[24] M. Liu, M. B. Johnston, H. J. Snaith, *Nature* **2013**, *501*, 395.
[25] C. Wehrenfennig, G. E. Eperon, M. B. Johnston, H. J. Snaith, L. M. Herz, *Adv. Mater.* **2013**, *26*, 1584.
[26] E. M. Hutter, J.-J. Hofman, M. L. Petrus, M. Moes, R. D. Abellón, P. Docampo, T. J. Savenije, *Adv. Energy Mater.* **2017**, *7*, 1602349.
[27] J. Burschka, N. Pellet, S.-J. Moon, R. Humphry-Baker, P. Gao, M. K. Nazeeruddin, M. Grätzel, *Nature* **2013**, *499*, 316.
[28] N. J. Jeon, J. H. Noh, W. S. Yang, Y. C. Kim, S. Ryu, J. Seo, S. Il Seok, *Nature* **2015**, *517*, 476.
[29] B. G. H. M. Groeneveld, M. Najafi, B. Steensma, S. Adjokatse, H.-H. Fang, F. Jahani, L. Qiu, G. H. ten Brink, J. C. Hummelen, M. A. Loi, *APL Mater.* **2017**, *5*, 076103.
[30] J. Liu, S. Lu, L. Zhu, X. Li, W. C. H. Choy, *Nanoscale* **2016**, *8*, 3638.
[31] S. Kazim, F. J. Ramos, P. Gao, M. K. Nazeeruddin, M. Gratzel, S. Ahmad, *Energy Environ. Sci.* **2015**, *8*, 1816.
[32] N. K. Noel, S. N. Habisreutinger, B. Wenger, M. T. Klug, M. T. Horantner, M. B. Johnston, R. J. Nicholas, D. T. Moore, H. J. Snaith, *Energy Environ. Sci.* **2017**, *10*, 145.
[33] P. Ganesan, K. Fu, P. Gao, I. Raabe, K. Schenk, R. Scopelliti, J. Luo, L. H. Wong, M. Gratzel, M. K. Nazeeruddin, *Energy Environ. Sci.* **2015**, *8*, 1986.
[34] Q. Han, Y. Bai, J. Liu, K. Du, T. Li, D. Ji, Y. Zhou, C. Cao, D. Shin, J. Ding, A. D. Franklin, J. T. Glass, J. Hu, M. J. Therien, J. Liu, D. B. Mitzi, *Energy Environ. Sci.* **2017**, *10*, 2365.
[35] J. Seo, S. Park, Y. Chan Kim, N. J. Jeon, J. H. Noh, S. C. Yoon, S. Il Seok, *Energy Environ. Sci.* **2014**, *7*, 2642.
[36] K. Aitola, K. Sveinbjornsson, J.-P. Correa-Baena, A. Kaskela, A. Abate, Y. Tian, E. M. J. Johansson, M. Gratzel, E. I. Kauppinen, A. Hagfeldt, G. Boschloo, *Energy Environ. Sci.* **2016**, *9*, 461.
[37] M. Saliba, T. Matsui, J.-Y. Seo, K. Domanski, J.-P. Correa-Baena, M. K. Nazeeruddin, S. M. Zakeeruddin, W. Tress, A. Abate, A. Hagfeldt, M. Gratzel, *Energy Environ. Sci.* **2016**, *9*, 1989.
[38] C. Momblona, L. Gil-Escrig, E. Bandiello, E. M. Hutter, M. Sessolo, K. Lederer, J. Blochwitz-Nimoth, H. J. Bolink, *Energy Environ. Sci.* **2016**, *9*, 3456.
[39] N. J. Jeon, J. H. Noh, Y. C. Kim, W. S. Yang, S. Ryu, S. Il Seok, *Nat. Mater.* **2014**, *13*, 897.
[40] G. E. Eperon, S. D. Stranks, C. Menelaou, M. B. Johnston, L. M. Herz, H. J. Snaith, *Energy Environ. Sci.* **2014**, *7*, 982.
[41] Q. Chen, H. Zhou, Z. Hong, S. Luo, H.-S. Duan, H.-H. Wang, Y. Liu, G. Li, Y. Yang, *J. Am. Chem. Soc.* **2014**, *136*, 622.
[42] D. P. McMeekin, G. Sadoughi, W. Rehman, G. E. Eperon, M. Saliba, M. T. Hörantner, A. Haghighirad, N. Sakai, L. Korte, B. Rech, M. B. Johnston, L. M. Herz, H. J. Snaith, *Science* **2016**, *351*, 151.
[43] I. C. Smith, E. T. Hoke, D. Solis-Ibarra, M. D. McGehee, H. I. Karunadasa, *Angew. Chem.* **2014**, *126*, 11414.
[44] N. Pellet, P. Gao, G. Gregori, T.-Y. Yang, M. K. Nazeeruddin, J. Maier, M. Gratzel, *Angew. Chem., Int. Ed.* **2014**, *53*, 3151.
[45] M. Khalid, S. B. Sankar, A. Aram, *Adv. Energy Mater.* **2015**, *5*, 1500568.
[46] L. B. Xiong, M.-C. QIn, X.-Z. Zhao, G.-J. Fang, *Adv. Mater. Interfaces* **2016**, *3*, 1500799.
[47] Z. Hawash, L. K. Ono, Y. Qi, *Adv. Mater. Interfaces* **2016**, *3*, 1600117.
[48] Y. Jo, K. S. Oh, M. Kim, K.-H. Kim, H. Lee, C.-W. Lee, D. S. Kim, *Adv. Mater. Interfaces* **2016**, *3*, 1500768.
[49] S. Shao, M. Abdu-Aguye, L. Qiu, L.-H. Lai, J. Liu, S. Adjokatse, F. Jahani, M. E. Kamminga, G. H. ten Brink, T. T. M. Palstra, B. J. Kooi, J. C. Hummelen, M. Antonietta Loi, *Energy Environ. Sci.* **2016**, *9*, 2444.

[50] S. Shao, J. Liu, H.-H. Fang, L. Qiu, G. H. ten Brink, J. C. Hummelen, L. J. A. Koster, M. A. Loi, *Adv. Energy Mater.* **2017**, *7*, 1701305.
[51] S. Shao, Z. Chen, H.-H. Fang, G. H. ten Brink, D. Bartesaghi, S. Adjokatse, L. J. A. Koster, B. J. Kooi, A. Facchetti, M. A. Loi, *J. Mater. Chem. A* **2016**, *4*, 2419.
[52] S. Shao, M. Abdu-Aguye, T. Sherkar, H.-H. Fang, S. Adjokatse, G. ten Brink, B. J. Kooi, L. Koster, M. A. Loi, *Adv. Funct. Mater.* **2016**, *26*, 8094.
[53] G.-W. Kim, G. Kang, M. Malekshahi Byranvand, G.-Y. Lee, T. Park, *ACS Appl. Mater. Interfaces* **2017**, *9*, 27720.
[54] F. Giordano, A. Abate, J. P. Correa Baena, M. Saliba, T. Matsui, S. H. Im, S. M. Zakeeruddin, M. K. Nazeeruddin, A. Hagfeldt, M. Graetzel, *Nat. Commun.* **2016**, *7*, 10379.
[55] A. Mei, X. Li, L. Liu, Z. Ku, T. Liu, Y. Rong, M. Xu, M. Hu, J. Chen, Y. Yang, M. Grätzel, H. Han, *Science* **2014**, *345*, 295.
[56] "Best Research-Cell Efficiency Chart | Photovoltaic Research | NREL," https://www.nrel.gov/pv/cell-efficiency.html (accessed: November 2019).
[57] S. Wang, T. Sakurai, W. Wen, Y. Qi, *Adv. Mater. Interfaces* **2018**, *5*, 1800260.
[58] Q.-D. Ou, C. Li, Q.-K. Wang, Y.-Q. Li, J.-X. Tang, *Adv. Mater. Interfaces* **2017**, *4*, 1600694.
[59] P. Schulz, D. Cahen, A. Kahn, *Chem. Rev.* **2019**, *119*, 3349.
[60] E. M. Hutter, G. E. Eperon, S. D. Stranks, T. J. Savenije, *J. Phys. Chem. Lett.* **2015**, *6*, 3082.
[61] S. D. Stranks, V. M. Burlakov, T. Leijtens, J. M. Ball, A. Goriely, H. J. Snaith, *Phys. Rev. Appl.* **2014**, *2*, 034007.
[62] H.-H. Fang, R. Raissa, M. Abdu-Aguye, S. Adjokatse, G. R. Blake, J. Even, M. A. Loi, *Adv. Funct. Mater.* **2015**, *25*, 2378.
[63] C. S. Ponseca, E. M. Hutter, P. Piatkowski, B. Cohen, T. Pascher, A. Douhal, A. Yartsev, V. Sundström, T. J. Savenije, *J. Am. Chem. Soc.* **2015**, *137*, 16043.
[64] W. Shockley, W. T. Read, *Phys. Rev.* **1952**, *87*, 835.
[65] S. Shao, Y. Cui, H. Duim, X. Qiu, J. Dong, G. H. ten Brink, G. Portale, R. C. Chiechi, S. Zhang, J. Hou, M. A. Loi, *Adv. Mater.* **2018**, *30*, 1803703.
[66] E. L. Unger, E. T. Hoke, C. D. Bailie, W. H. Nguyen, A. R. Bowring, T. Heumuller, M. G. Christoforo, M. D. McGehee, *Energy Environ. Sci.* **2014**, *7*, 3690.
[67] C. Zhao, B. Chen, X. Qiao, L. Luan, K. Lu, B. Hu, *Adv. Energy Mater.* **2015**, *5*, 1500279.
[68] Y. Deng, Z. Xiao, J. Huang, *Adv. Energy Mater.* **2015**, *5*, 1500721.
[69] W.-J. Yin, T. Shi, Y. Yan, *Appl. Phys. Lett.* **2014**, *104*, 063903.
[70] D. W. de Quilettes, S. M. Vorpahl, S. D. Stranks, H. Nagaoka, G. E. Eperon, M. E. Ziffer, H. J. Snaith, D. S. Ginger, *Science* **2015**, *348*, 683.
[71] S. Shao, J. Dong, H. Duim, G. H. ten Brink, G. R. Blake, G. Portale, M. A. Loi, *Nano Energy* **2019**, *60*, 810.
[72] J. S. Yun, J. Seidel, J. Kim, A. M. Souflani, S. Huang, J. Lau, N. J. Jeon, S. II Seok, M. A. Green, A. Ho-Baillie, *Adv. Energy Mater.* **2016**, *6*, 1600330.
[73] T. S. Sherkar, C. Momblona, L. Gil-Escrig, J. Ávila, M. Sessolo, H. J. Bolink, L. J. A. Koster, *ACS Energy Lett.* **2017**, *2*, 1214.
[74] W. Nie, H. Tsai, R. Asadpour, J.-C. Blancon, A. J. Neukirch, G. Gupta, J. J. Crochet, M. Chhowalla, S. Tretiak, M. A. Alam, H.-L. Wang, A. D. Mohite, *Science* **2015**, *347*, 522.
[75] R. Singh, S. R. Suranagi, M. Kumar, V. K. Shukla, *J. Appl. Phys.* **2017**, *122*, 235302.
[76] C. Bi, Q. Wang, Y. Shao, Y. Yuan, Z. Xiao, J. Huang, *Nat. Commun.* **2015**, *6*, 7747.
[77] X. Qi, Y. Zhang, Q. Ou, S. T. Ha, C.-W. Qiu, H. Zhang, Y.-B. Cheng, Q. Xiong, Q. Bao, *Small* **2018**, *14*, 1800682.
[78] S. Chen, G. Shi, *Adv. Mater.* **2017**, *29*, 1605448.
[79] C. Huang, W. Fu, C.-Z. Li, Z. Zhang, W. Qiu, M. Shi, P. Heremans, A. K.-Y. Jen, H. Chen, *J. Am. Chem. Soc.* **2016**, *138*, 2528.
[80] Z. Wu, S. Bai, J. Xiang, Z. Yuan, Y. Yang, W. Cui, X. Gao, Z. Liu, Y. Jin, B. Sun, *Nanoscale* **2014**, *6*, 10505.
[81] Y. Bai, H. Chen, S. Xiao, Q. Xue, T. Zhang, Z. Zhu, Q. Li, C. Hu, Y. Yang, Z. Hu, F. Huang, K. S. Wong, H.-L. Yip, S. Yang, *Adv. Funct. Mater.* **2016**, *26*, 2950.
[82] Y. Ogomi, A. Morita, S. Tsukamoto, T. Saitho, Q. Shen, T. Toyoda, K. Yoshino, S. S. Pandey, T. Ma, S. Hayase, *J. Phys. Chem. C* **2014**, *118*, 16651.
[83] L. Zuo, Z. Gu, T. Ye, W. Fu, G. Wu, H. Li, H. Chen, *J. Am. Chem. Soc.* **2015**, *137*, 2674.
[84] L. Liu, A. Mei, T. Liu, P. Jiang, Y. Sheng, L. Zhang, H. Han, *J. Am. Chem. Soc.* **2015**, *137*, 1790.
[85] G. Yang, C. Wang, H. Lei, X. Zheng, P. Qin, L. Xiong, X. Zhao, Y. Yan, G. Fang, *J. Mater. Chem. A* **2017**, *5*, 1658.
[86] I. Zarazua, J. Bisquert, G. Garcia-Belmonte, *J. Phys. Chem. Lett.* **2016**, *7*, 525.
[87] J. C. Brauer, Y. H. Lee, M. K. Nazeeruddin, N. Banerji, *J. Phys. Chem. Lett.* **2015**, *6*, 3675.
[88] S. Li, F. Ding, M. Shi, C.-Z. Li, A. K.-Y. Jen, H. Chen, *Adv. Energy Mater.* **2017**, *7*, 1700012.
[89] Y. G. Kim, K. C. Kwon, Q. Van Le, K. Hong, H. W. Jang, S. Y. Kim, *J. Power Sources* **2016**, *319*, 1.
[90] B. Peng, G. Yu, Y. Zhao, Q. Xu, G. Xing, X. Liu, D. Fu, B. Liu, J. R. S. Tan, W. Tang, H. Lu, J. Xie, L. Deng, T. C. Sum, K. P. Loh, *ACS Nano* **2016**, *10*, 6383.
[91] J. T.-W. Wang, J. M. Ball, E. M. Barea, A. Abate, J. A. Alexander-Webber, J. Huang, M. Saliba, I. Mora-Sero, J. Bisquert, H. J. Snaith, R. J. Nicholas, *Nano Lett.* **2014**, *14*, 724.
[92] Z. Zhu, J. Ma, Z. Wang, C. Mu, Z. Fan, L. Du, Y. Bai, L. Fan, H. Yan, D. L. Phillips, S. Yang, *J. Am. Chem. Soc.* **2014**, *136*, 3760.
[93] H. Yu, X. Liu, Y. Xia, Q. Dong, K. Zhang, Z. Wang, Y. Zhou, B. Song, Y. Li, *J. Mater. Chem. A* **2016**, *4*, 321.
[94] L. Zuo, Q. Chen, N. De Marco, Y.-T. Hsieh, H. Chen, P. Sun, S.-Y. Chang, H. Zhao, S. Dong, Y. Yang, *Nano Lett.* **2017**, *17*, 269.
[95] H. W. Qiao, S. Yang, Y. Wang, X. Chen, T. Y. Wen, L. J. Tang, Q. Cheng, Y. Hou, H. Zhao, H. G. Yang, *Adv. Mater.* **2019**, *31*, 1804217.
[96] P. Cui, D. Wei, J. Ji, H. Huang, E. Jia, S. Dou, T. Wang, W. Wang, M. Li, *Nat. Energy* **2019**, *4*, 150.
[97] W.-Q. Wu, Q. Wang, Y. Fang, Y. Shao, S. Tang, Y. Deng, H. Lu, Y. Liu, T. Li, Z. Yang, A. Gruverman, J. Huang, *Nat. Commun.* **2018**, *9*, 1625.
[98] S. Ravishankar, S. Gharibzadeh, C. Roldán-Carmona, G. Grancini, Y. Lee, M. Ralaiarisoa, A. M. Asiri, N. Koch, J. Bisquert, M. K. Nazeeruddin, *Joule* **2018**, *2*, 788.
[99] R. A. Belisle, P. Jain, R. Prasanna, T. Leijtens, M. D. McGehee, *ACS Energy Lett.* **2016**, *1*, 556.
[100] J. Jiménez-López, W. Cambarau, L. Cabau, E. Palomares, *Sci. Rep.* **2017**, *7*, 6101.
[101] B. Dänekamp, N. Droseros, D. Tsokkou, V. Brehm, P. P. Boix, M. Sessolo, N. Banerji, H. J. Bolink, *J. Mater. Chem. C* **2019**, *7*, 523.
[102] D. W. deQuilettes, S. M. Vorpahl, S. D. Stranks, H. Nagaoka, G. E. Eperon, M. E. Ziffer, H. J. Snaith, D. S. Ginger, *Science* **2015**, *348*, 683.
[103] E. J. Juarez-Perez, M. Wuβler, F. Fabregat-Santiago, K. Lakus-Wollny, E. Mankel, T. Mayer, W. Jaegermann, I. Mora-Sero, *J. Phys. Chem. Lett.* **2014**, *5*, 680.
[104] E. Ghahremanirad, A. Bou, S. Olyaee, J. Bisquert, *J. Phys. Chem. Lett.* **2017**, *8*, 1402.
[105] I. Zarazua, G. Han, P. P. Boix, S. Mhaisalkar, F. Fabregat-Santiago, I. Mora-Seró, J. Bisquert, G. Garcia-Belmonte, *J. Phys. Chem. Lett.* **2016**, *7*, 5105.
[106] Y. Shao, Z. Xiao, C. Bi, Y. Yuan, J. Huang, *Nat. Commun.* **2014**, *5*, 5784.
[107] N. K. Noel, A. Abate, S. D. Stranks, E. S. Parrott, V. M. Burlakov, A. Goriely, H. J. Snaith, *ACS Nano* **2014**, *8*, 9815.

[108] A. Abate, M. Saliba, D. J. Hollman, S. D. Stranks, K. Wojciechowski, R. Avolio, G. Grancini, A. Petrozza, H. J. Snaith, *Nano Lett.* **2014**, *14*, 3247.
[109] C. Tao, S. Neutzner, L. Colella, S. Marras, A. R. Srimath Kandada, M. Gandini, M. De Bastiani, G. Pace, L. Manna, M. Caironi, C. Bertarelli, A. Petrozza, *Energy Environ. Sci.* **2015**, *8*, 2365.
[110] H. Tan, A. Jain, O. Voznyy, X. Lan, F. P. García de Arquer, J. Z. Fan, R. Quintero-Bermudez, M. Yuan, B. Zhang, Y. Zhao, F. Fan, P. Li, L. N. Quan, Y. Zhao, Z.-H. Lu, Z. Yang, S. Hoogland, E. H. Sargent, *Science* **2017**,*355*, 722.
[111] Y. Cui, B. Xu, B. Yang, H. Yao, S. Li, J. Hou, *Macromolecules* **2016**, *49*, 8126.
[112] J. A. Christians, R. C. M. Fung, P. V. Kamat, *J. Am. Chem. Soc.* **2014**, *136*, 758.
[113] H. Peng, W. Sun, Y. Li, S. Ye, H. Rao, W. Yan, H. Zhou, Z. Bian, C. Huang, *Nano Res.* **2016**, *9*, 2960.
[114] Z. Zhu, C.-C. Chueh, F. Lin, A. K.-Y. Jen, *Adv. Sci.* **2016**, *3*, 1600027.
[115] W. Chen, Y. Wu, Y. Yue, J. Liu, W. Zhang, X. Yang, H. Chen, E. Bi, I. Ashraful, M. Grätzel, L. Han, *Science* **2015**, *350*, 944.
[116] J. W. Jung, C.-C. Chueh, A. K.-Y. Jen, *Adv. Mater.* **2015**, *27*, 7874.
[117] W. Chen, F.-Z. Liu, X.-Y. Feng, A. B. Djurisic, W. K. Chen, Z.-B. He, *Adv. Energy Mater.* **2017**, *7*, 1700722.
[118] J. W. Jung, C.-C. Chueh, A. K.-Y. Jen, *Adv. Mater.* **2015**, *27*, 7874.
[119] T. Leijtens, J. Lim, J. Teuscher, T. Park, H. J. Snaith, *Adv. Mater.* **2013**, *25*, 3227.
[120] U. Bach, D. Lupo, P. Comte, J. E. Moser, F. Weissörtel, J. Salbeck, H. Spreitzer, M. Grätzel, *Nature* **1998**, *395*, 583.
[121] J. H. Heo, S. H. Im, J. H. Noh, T. N. Mandal, C.-S. Lim, J. A. Chang, Y. H. Lee, H. Kim, A. Sarkar, N. K., M. Gratzel, S. Il Seok, *Nat. Photonics* **2013**, *7*, 486.
[122] K. Wojciechowski, T. Leijtens, S. Siprova, C. Schlueter, M. T. Hörantner, J. T.-W. Wang, C.-Z. Li, A. K.-Y. Jen, T.-L. Lee, H. J. Snaith, *J. Phys. Chem. Lett.* **2015**, *6*, 2399.
[123] J.-H. Bae, Y.-J. Noh, M. Kang, D.-Y. Kim, H.-B. Kim, S.-H. Oh, J.-M. Yun, S.-I. Na, *RSC Adv.* **2016**, *6*, 64962.
[124] S. S. Kim, S. Bae, W. H. Jo, *Chem. Commun.* **2015**, *51*, 17413.
[125] C. Kuang, G. Tang, T. Jiu, H. Yang, H. Liu, B. Li, W. Luo, X. Li, W. Zhang, F. Lu, J. Fang, Y. Li, *Nano Lett.* **2015**, *15*, 2756.
[126] J.-S. Yeo, R. Kang, S. Lee, Y.-J. Jeon, N. Myoung, C.-L. Lee, D.-Y. Kim, J.-M. Yun, Y.-H. Seo, S.-S. Kim, S.-I. Na, *Nano Energy* **2015**, *12*, 96.
[127] J. Kim, M. A. Mat Teridi, A. R. bin Mohd Yusoff, J. Jang, *Sci. Rep.* **2016**, *6*, 27773.
[128] J. Liu, S. Shao, B. Meng, G. Fang, Z. Xie, L. Wang, X. Li, *Appl. Phys. Lett.* **2012**, *100*, 213906.
[129] J. Wang, M. Qin, H. Tao, W. Ke, Z. Chen, J. Wan, P. Qin, L. Xiong, H. Lei, H. Yu, G. Fang, *Appl. Phys. Lett.* **2015**, *106*, 121104.
[130] X. Zhang, Z. Bao, X. Tao, H. Sun, W. Chen, X. Zhou, *RSC Adv.* **2014**, *4*, 64001.
[131] S. S. Shin, E. J. Yeom, W. S. Yang, S. Hur, M. G. Kim, J. Im, J. Seo, J. H. Noh, S. Il Seok, *Science* **2017**, *356*, 167.
[132] N. Arora, M. I. Dar, A. Hinderhofer, N. Pellet, F. Schreiber, S. M. Zakeeruddin, M. Grätzel, *Science* **2017**, *358*, 768.
[133] B. Cai, Y. Xing, Z. Yang, W.-H. Zhang, J. Qiu, *Energy Environ. Sci.* **2013**, *6*, 1480.
[134] C. Bert, B. Linny, D. D. Christopher, D. Jan, M. Jean, B. Hans-Gerd, *Adv. Mater.* **2013**, *26*, 2041.
[135] A. Dubey, N. Adhikari, S. Venkatesan, S. Gu, D. Khatiwada, Q. Wang, L. Mohammad, M. Kumar, Q. Qiao, *Sol. Energy Mater. Sol. Cells* **2016**, *145*, 193.
[136] G.-W. Kim, G. Kang, J. Kim, G.-Y. Lee, H. Il Kim, L. Pyeon, J. Lee, T. Park, *Energy Environ. Sci.* **2016**, *9*, 2326.
[137] J. Liu, Y. Wu, C. Qin, X. Yang, T. Yasuda, A. Islam, K. Zhang, W. Peng, W. Chen, L. Han, *Energy Environ. Sci.* **2014**, *7*, 2963.
[138] G. Gong, N. Zhao, D. Ni, J. Chen, Y. Shen, M. Wang, G. Tu, *J. Mater. Chem. A* **2016**, *4*, 3661.
[139] P. Qin, H. Kast, M. K. Nazeeruddin, S. M. Zakeeruddin, A. Mishra, P. Bauerle, M. Gratzel, *Energy Environ. Sci.* **2014**, *7*, 2981.
[140] C. Steck, M. Franckevicius, S. M. Zakeeruddin, A. Mishra, P. Bauerle, M. Gratzel, *J. Mater. Chem. A* **2015**, *3*, 17738.
[141] M. Cheng, C. Chen, X. Yang, J. Huang, F. Zhang, B. Xu, L. Sun, *Chem. Mater.* **2015**, *27*, 1808.
[142] C. Ming, X. Bo, C. Cheng, Y. Xichuan, Z. Fuguo, T. Qin, H. Yong, K. Lars, S. Licheng, *Adv. Energy Mater.* **2015**, *5*, 1401720.
[143] L. Zheng, Y.-H. Chung, Y. Ma, L. Zhang, L. Xiao, Z. Chen, S. Wang, B. Qu, Q. Gong, *Chem. Commun.* **2014**, *50*, 11196.
[144] Y. Liu, Q. Chen, H.-S. Duan, H. Zhou, Y. (Michael) Yang, H. Chen, S. Luo, T.-B. Song, L. Dou, Z. Hong, Y. Yang, *J. Mater. Chem. A* **2015**, *3*, 11940.
[145] L. Yongsheng, H. Ziruo, C. Qi, C. Huajun, C. Wei-Hsuan, Y. Y. (Michael), S. Tze-Bin, Y. Yang, *Adv. Mater.* **2015**, *28*, 440.
[146] S. Shao, K. Zheng, K. Zidek, P. Chabera, T. Pullerits, F. Zhang, *Sol. Energy Mater. Sol. Cells* **2013**, *118*, 43.
[147] S. Shao, J. Liu, B. Zhang, Z. Xie, L. Wang, *Appl. Phys. Lett.* **2011**, *98*, 203304.
[148] S. Shao, F. Liu, Z. Xie, L. Wang, *J. Phys. Chem. C* **2010**, *114*, 9161.
[149] Z. Peng, W. Jiang, Z. Ting, W. Yafei, L. Detao, C. Hao, J. Long, L. Chunhua, A. Waseem, C. Z. David, L. Shibin, *Adv. Mater.* **2018**, *30*, 1703737.
[150] W. Ke, G. Fang, Q. Liu, L. Xiong, P. Qin, H. Tao, J. Wang, H. Lei, B. Li, J. Wan, G. Yang, Y. Yan, *J. Am. Chem. Soc.* **2015**, *137*, 6730.
[151] Q. Jiang, L. Zhang, H. Wang, X. Yang, J. Meng, H. Liu, Z. Yin, J. Wu, X. Zhang, J. You, *Nat. Energy* **2016**, *2*, 16177.
[152] C. Wang, D. Zhao, C. R. Grice, W. Liao, Y. Yu, A. Cimaroli, N. Shrestha, P. J. Roland, J. Chen, Z. Yu, P. Liu, N. Cheng, R. J. Ellingson, X. Zhao, Y. Yan, *J. Mater. Chem. A* **2016**, *4*, 12080.
[153] E. H. Anaraki, A. Kermanpur, L. Steier, K. Domanski, T. Matsui, W. Tress, M. Saliba, A. Abate, M. Gratzel, A. Hagfeldt, J.-P. Correa-Baena, *Energy Environ. Sci.* **2016**, *9*, 3128.
[154] S. Ameen, M. S. Akhtar, H.-K. Seo, M. K. Nazeeruddin, H.-S. Shin, *J. Phys. Chem. C* **2015**, *119*, 10379.
[155] J. Ciro, S. Mesa, J. I. Uribe, M. A. Mejia-Escobar, D. Ramirez, J. F. Montoya, R. Betancur, H.-S. Yoo, N.-G. Park, F. Jaramillo, *Nanoscale* **2017**, *9*, 9440.
[156] J. You, L. Meng, T.-B. Song, T.-F. Guo, Y. (Michael) Yang, W.-H. Chang, Z. Hong, H. Chen, H. Zhou, Q. Chen, Y. Liu, N. De Marco, Y. Yang, *Nat. Nanotechnol.* **2016**, *11*, 75.
[157] X. Zhao, H. Shen, Y. Zhang, X. Li, X. Zhao, M. Tai, J. Li, J. Li, X. Li, H. Lin, *ACS Appl. Mater. Interfaces* **2016**, *8*, 7826.
[158] Y. Shizhong, L. Shudi, R. Kuankuan, L. Kong, A. Muhammad, C. Dawei, W. Zhijie, L. Yong, Q. Shengchun, W. Zhanguo, *Small* **2017**, *13*, 1700007.
[159] W. Yan, Y. Li, Y. Li, S. Ye, Z. Liu, S. Wang, Z. Bian, C. Huang, *Nano Res.* **2015**, *8*, 2474.
[160] P.-W. Liang, C.-C. Chueh, S. T. Williams, A. K.-Y. Jen, *Adv. Energy Mater.* **2015**, *5*, 1402321.
[161] X. Liu, M. Lei, Y. Zhou, B. Song, Y. Li, *Appl. Phys. Lett.* **2015**, *107*, 063901.
[162] H. Azimi, T. Ameri, H. Zhang, Y. Hou, C. O. R. Quiroz, J. Min, M. Hu, Z.-G. Zhang, T. Przybilla, G. J. Matt, E. Spiecker, Y. Li, C. J. Brabec, *Adv. Energy Mater.* **2015**, *5*, 1401692.
[163] H. Zhang, H. Azimi, Y. Hou, T. Ameri, T. Przybilla, E. Spiecker, M. Kraft, U. Scherf, C. J. Brabec, *Chem. Mater.* **2014**, *26*, 5190.
[164] J. Min, Z.-G. Zhang, Y. Hou, C. O. Ramirez Quiroz, T. Przybilla, C. Bronnbauer, F. Guo, K. Forberich, H. Azimi, T. Ameri, E. Spiecker, Y. Li, C. J. Brabec, *Chem. Mater.* **2015**, *27*, 227.
[165] W. Chen, L. Xu, X. Feng, J. Jie, Z. He, *Adv. Mater.* **2017**, *29*, 1603923.

[166] Q. Xue, Z. Hu, J. Liu, J. Lin, C. Sun, Z. Chen, C. Duan, J. Wang, C. Liao, W. M. Lau, F. Huang, H.-L. Yip, Y. Cao, *J. Mater. Chem. A* **2014**, *2*, 19598.
[167] L. K. Ono, S. R. Raga, S. Wang, Y. Kato, Y. Qi, *J. Mater. Chem. A* **2015**, *3*, 9074.
[168] W. Tress, N. Marinova, T. Moehl, S. M. Zakeeruddin, M. K. Nazeeruddin, M. Gratzel, *Energy Environ. Sci.* **2015**, *8*, 995.
[169] J. Wei, Y. Zhao, H. Li, G. Li, J. Pan, D. Xu, Q. Zhao, D. Yu, *J. Phys. Chem. Lett.* **2014**, *5*, 3937.
[170] M. Sajedi Alvar, M. Kumar, P. W. M. Blom, G.-J. A. H. Wetzelaer, K. Asadi, *AIP Adv.* **2017**, *7*, 095110.
[171] J. Beilsten-Edmands, G. E. Eperon, R. D. Johnson, H. J. Snaith, P. G. Radaelli, *Appl. Phys. Lett.* **2015**, *106*, 173502.
[172] A. Walsh, D. O. Scanlon, S. Chen, X. G. Gong, S.-H. Wei, *Angew. Chem., Int. Ed.* **2015**, *54*, 1791.
[173] Y. Luo, P. Khoram, S. Brittman, Z. Zhu, B. Lai, S. P. Ong, E. C. Garnett, D. P. Fenning, *Adv. Mater.* **2017**, *29*, 1703451.
[174] Y. Yuan, Q. Wang, Y. Shao, H. Lu, T. Li, A. Gruverman, J. Huang, *Adv. Energy Mater.* **2015**, *6*, 1501803.
[175] H. Lee, S. Gaiaschi, P. Chapon, A. Marronnier, H. Lee, J.-C. Vanel, D. Tondelier, J.-E. Bourée, Y. Bonnassieux, B. Geffroy, *ACS Energy Lett.* **2017**, *2*, 943.
[176] P. Calado, A. M. Telford, D. Bryant, X. Li, J. Nelson, B. C. O'Regan, P. R. Barnes, *Nat. Commun.* **2016**, *7*, 13831.
[177] Y. Wu, H. Shen, D. Walter, D. Jacobs, T. Duong, J. Peng, L. Jiang, Y.-B. Cheng, K. Weber, *Adv. Funct. Mater.* **2016**, *26*, 6807.
[178] S. van Reenen, M. Kemerink, H. J. Snaith, *J. Phys. Chem. Lett.* **2015**, *6*, 3808.
[179] T. Zhang, M. Long, K. Yan, M. Qin, X. Lu, X. Zeng, C. C. Cheng, K. S. Wang, P. Liu, W. Xie, J. Xu, *Adv. Energy Mater.* **2017**, *7*, 1700118.
[180] J. Peng, Y. Wu, W. Ye, D. A. Jacobs, H. Shen, X. Fu, Y. Wan, T. Duong, N. Wu, C. Barugkin, H. T. Nguyen, D. Zhong, J. Li, T. Lu, Y. Liu, M. N. Lockrey, K. J. Weber, K. R. Catchpole, T. P. White, *Energy Environ. Sci.* **2017**, *10*, 1792.
[181] K. Wojciechowski, S. D. Stranks, A. Abate, G. Sadoughi, A. Sadhanala, N. Kopidakis, G. Rumbles, C.-Z. Li, R. H. Friend, A. K.-Y. Jen, H. J. Snaith, *ACS Nano* **2014**, *8*, 12701.
[182] H. Nagaoka, F. Ma, D. W. deQuilettes, S. M. Vorpahl, M. S. Glaz, A. E. Colbert, M. E. Ziffer, D. S. Ginger, *J. Phys. Chem. Lett.* **2015**, *6*, 669.
[183] G. Yang, H. Lei, H. Tao, X. Zheng, J. Ma, Q. Liu, P. Qin, Z. Chen, M. Qin, X. Lu, Y. Yan, G. Fang, *Small* **2017**, *13*, 1601769.
[184] Z. Li, C. Xiao, Y. Yang, S. P. Harvey, D. H. Kim, J. A. Christians, M. Yang, P. Schulz, S. U. Nanayakkara, C.-S. Jiang, J. M. Luther, J. J. Berry, M. C. Beard, M. M. Al-Jassim, K. Zhu, *Energy Environ. Sci.* **2017**, *10*, 1234.
[185] Z. Xiao, Y. Yuan, Y. Shao, Q. Wang, Q. Dong, C. Bi, P. Sharma, A. Gruverman, J. Huang, *Nat. Mater.* **2015**, *14*, 193.
[186] M. Shirayama, M. Kato, T. Miyadera, T. Sugita, T. Fujiseki, S. Hara, H. Kadowaki, D. Murata, M. Chikamatsu, H. Fujiwara, *J. Appl. Phys.* **2016**, *119*, 115501.
[187] J. Yang, B. D. Siempelkamp, D. Liu, T. L. Kelly, *ACS Nano* **2015**, *9*, 1955.
[188] S. Shao, J. Liu, J. Bergqvist, S. Shi, C. Veit, U. Würfel, Z. Xie, F. Zhang, *Adv. Energy Mater.* **2013**, *3*, 349.
[189] S. N. Habisreutinger, T. Leijtens, G. E. Eperon, S. D. Stranks, R. J. Nicholas, H. J. Snaith, *Nano Lett.* **2014**, *14*, 5561.
[190] Z. Wang, Q. Ou, Y. Zhang, Q. Zhang, H. Y. Hoh, Q. Bao, *ACS Appl. Mater. Interfaces* **2018**, *10*, 24258.
[191] H. Chen, Y. Hou, C. E. Halbig, S. Chen, H. Zhang, N. Li, F. Guo, X. Tang, N. Gasparini, I. Levchuk, S. Kahmann, C. O. Ramirez Quiroz, A. Osvet, S. Eigler, C. J. Brabec, *J. Mater. Chem. A* **2016**, *4*, 11604.
[192] Y. Bai, Q. Dong, Y. Shao, Y. Deng, Q. Wang, L. Shen, D. Wang, W. Wei, J. Huang, *Nat. Commun.* **2016**, *7*, 12806.
[193] A. Savva, I. Burgués-Ceballos, S. A. Choulis, *Adv. Energy Mater.* **2016**, *6*, 1600285.
[194] Y. Li, X. Xu, C. Wang, B. Ecker, J. Yang, J. Huang, Y. Gao, *J. Phys. Chem. C* **2017**, *121*, 3904.
[195] D. Bryant, N. Aristidou, S. Pont, I. Sanchez-Molina, T. Chotchuna ngatchaval, S. Wheeler, J. R. Durrant, S. A. Haque, *Energy Environ. Sci.* **2016**, *9*, 1655.
[196] T. Leijtens, G. E. Eperon, S. Pathak, A. Abate, M. M. Lee, H. J. Snaith, *Nat. Commun.* **2013**, *4*, 2885.
[197] W. Li, W. Zhang, S. Van Reenen, R. J. Sutton, J. Fan, A. A. Haghighirad, M. B. Johnston, L. Wang, H. J. Snaith, *Energy Environ. Sci.* **2016**, *9*, 490.
[198] H.-H. Fang, J. Yang, S. Tao, S. Adjokatse, M. E. Kamminga, J. Ye, G. R. Blake, J. Even, M. A. Loi, *Adv. Funct. Mater.* **2018**, *28*, 1800305.
[199] E. J. Juarez-Perez, Z. Hawash, S. R. Raga, L. K. Ono, Y. Qi, *Energy Environ. Sci.* **2016**, *9*, 3406.
[200] T. Baikie, Y. Fang, J. M. Kadro, M. Schreyer, F. Wei, S. G. Mhaisalkar, M. Graetzel, T. J. White, *J. Mater. Chem. A* **2013**, *1*, 5628.
[201] L. Dimesso, M. Dimamay, M. Hamburger, W. Jaegermann, *Chem. Mater.* **2014**, *26*, 6762.
[202] L. N. Quan, M. Yuan, R. Comin, O. Voznyy, E. M. Beauregard, S. Hoogland, A. Buin, A. R. Kirmani, K. Zhao, A. Amassian, D. H. Kim, E. H. Sargent, *J. Am. Chem. Soc.* **2016**, *138*, 2649.
[203] Z. Fan, H. Xiao, Y. Wang, Z. Zhao, Z. Lin, H.-C. Cheng, S.-J. Lee, G. Wang, Z. Feng, W. A. Goddard, Y. Huang, X. Duan, *Joule* **2017**, *1*, 548.
[204] B. Conings, J. Drijkoningen, N. Gauquelin, A. Babayigit, J. D'Haen, L. D'Olieslaeger, A. Ethirajan, J. Verbeeck, J. Manca, E. Mosconi, F. De Angelis, H.-G. Boyen, *Adv. Energy Mater.* **2015**, *5*, 1500477.
[205] B. Philippe, B.-W. Park, R. Lindblad, J. Oscarsson, S. Ahmadi, E. M. J. Johansson, H. Rensmo, *Chem. Mater.* **2015**, *27*, 1720.
[206] N.-K. Kim, Y. H. Min, S. Noh, E. Cho, G. Jeong, M. Joo, S.-W. Ahn, J. S. Lee, S. Kim, K. Ihm, H. Ahn, Y. Kang, H.-S. Lee, D. Kim, *Sci. Rep.* **2017**, *7*, 4645.
[207] X. Zhao, H.-S. Kim, J.-Y. Seo, N.-G. Park, *ACS Appl. Mater. Interfaces* **2017**, *9*, 7148.
[208] J. Yang, B. D. Siempelkamp, E. Mosconi, F. De Angelis, T. L. Kelly, *Chem. Mater.* **2015**, *27*, 4229.
[209] M. M. Tavakoli, R. Tavakoli, Z. Nourbakhsh, A. Waleed, U. S. Virk, Z. Fan, *Adv. Mater. Interfaces* **2016**, *3*, 1500790.
[210] K. Domanski, J.-P. Correa-Baena, N. Mine, M. K. Nazeeruddin, A. Abate, M. Saliba, W. Tress, A. Hagfeldt, M. Grätzel, *ACS Nano* **2016**, *10*, 6306.
[211] Y. Kato, L. Y. Ono, M. V. Lee, S. Wang, S. R. Raga, Y. Qi, *Adv. Mater. Interfaces* **2015**, *2*, 1500195.
[212] A. Guerrero, J. You, C. Aranda, Y. S. Kang, G. Garcia-Belmonte, H. Zhou, J. Bisquert, Y. Yang, *ACS Nano* **2016**, *10*, 218.
[213] C. Besleaga, L. E. Abramiuc, V. Stancu, A. G. Tomulescu, M. Sima, L. Trinca, N. Plugaru, L. Pintilie, G. A. Nemnes, M. Iliescu, H. G. Svavarsson, A. Manolescu, I. Pintilie, *J. Phys. Chem. Lett.* **2016**, *7*, 5168.
[214] Y. Han, S. Meyer, Y. Dkhissi, K. Weber, J. M. Pringle, U. Bach, L. Spiccia, Y.-B. Cheng, *J. Mater. Chem. A* **2015**, *3*, 8139.
[215] H. Back, G. Kim, J. Kim, J. Kong, T. K. Kim, H. Kang, H. Kim, J. Lee, S. Lee, K. Lee, *Energy Environ. Sci.* **2016**, *9*, 1258.